

SCoBi-Veg: A Generalized Bistatic Scattering Model of Reflectometry from Vegetation for Signals of Opportunity Applications

Mehmet Kurum ⁽¹⁾, Manohar Deshpande ⁽²⁾, Alicia T. Joseph ⁽³⁾,
Peggy E. O'Neill ⁽³⁾, Roger H. Lang ⁽⁴⁾, Orhan Eroglu ⁽¹⁾

⁽¹⁾ Department of Electrical and Computer Engineering, Mississippi State University,
Mississippi State, MS, 39762

⁽²⁾ Microwave Instrument Technology Branch (Code 555), NASA Goddard Space Flight Center,
Greenbelt, MD 20771

⁽³⁾ Hydrological Sciences Laboratory (Code 617), NASA Goddard Space Flight Center,
Greenbelt, MD 20771

⁽⁴⁾ Department of Electrical and Computer Engineering, George Washington University,
Washington, DC, 20052

Abstract: SCoBi-Veg stands for Signals of opportunity Coherent Bistatic Vegetation model. It simulates polarimetric bistatic reflectometry of vegetated landscapes using a Monte Carlo scheme. The model is aimed at assessing the value of navigation and communication satellite Signals of Opportunity (SoOp) in a range of frequencies from P to S-bands for remote sensing of a number of geophysical land parameters such as soil moisture and biomass. A fully polarimetric expression for bistatic scattering from a vegetation canopy is first formulated for a general case and is then specialized to the practical case of ground-based/low altitude platforms with passive receivers overlooking vegetation using the signals transmitted from large distances. Using analytical wave theory in conjunction with distorted Born approximation, the transmit and receive antenna effects (i.e., polarization crosstalk/mismatch, orientation, altitude, etc.) are explicitly accounted for. The forward model developed here enables the understanding of the effect of different geophysical parameters and system configurations on the coherent and incoherent components of the reflected signatures. It can thus help developing robust inverse algorithm for extraction of soil moisture and biomass. The model is applied to P-band signals of geostationary communication satellites to describe polarimetric reflections from tree canopies as observed from down-looking platforms at various altitudes. The relative contributions of diffuse and specular scattering on total reflected power and reflectivity are quantified for various observing scenarios.

Index Terms– Signal of Opportunity, bistatic, vegetation, polarimetric, specular, diffuse

I. INTRODUCTION

Signal of Opportunity (SoOp) has emerged in recent years as a new domain of microwave remote sensing with great potential to realize the Earth Science community's need for global geophysical parameter retrieval at high spatiotemporal scales [1], [2]. The key principle of the SoOp approach is to receive and further extract information from free illuminators whose signal reflects off the Earth surface. Unlike traditional microwave remote sensing, the existing signal sources are exploited in bistatic configuration in which the transmitter and the receiver are separated by significant distance. SoOp systems are a powerful, cost-effective technology because they only require the development of a receiver, analysis software, and no on-board transmitter. SoOp concept has been widely used for collecting or modeling of Global Navigation Satellite Systems (GNSS) signal reflections over the ocean surface for estimating wind vectors or altimetry since the 1990s. It has been implemented in technology demonstration experiments (TechDemoSat-1 (TDS-1) [3], United Kingdom Disaster Monitoring Constellation (UK-DMC) [4]) and a dedicated ocean mission (Cyclone GNSS (CYGNSS) [5]) from space.

The application of GNSS reflectometry (GNSS-R) to other geophysical variables such as soil moisture, wetland extent, vegetation, and snow has also been studied from ground and airborne systems under several different measurement configurations [6]. For instance, interference patterns between direct and reflected signals are exploited using either geodetic or specifically designed GNSS receivers located on a tower to derive soil moisture over bare and vegetated surfaces [7], [8], [9], [10], [11]. In addition, airborne and balloon experiments have been used to evaluate the potential of GNSS-R methodologies for larger scale applications [12], [13]. Most

recently, the qualitative analysis of TDS-1 data over land, in conjunction with other satellite products such as soil moisture data from Soil Moisture Ocean Salinity (SMOS) level 3 and Normalized Difference Vegetation Index (NDVI) data from Moderate Resolution Imaging Spectroradiometer (MODIS) or Landsat, has demonstrated that the reflected signal has an extremely large dynamic range over land [14], [15], [16]. In addition, the large amount of land observations by the recent CYGNSS mission provides investigators opportunities to further infer the sensitivity of GNSS-R measurements to various land features from space.

There is increasing interest to extend these techniques originally developed for GNSS signals in L-band to digital transmissions from communication satellites in other bands [17]. For instance, SoOp methods have been applied to communication satellite broadcasts in S- and Ku-band and used to demonstrate remote sensing of ocean winds, significant wave height and sea surface height [18], [19]. The P-band signals transmitted by the Military Satellite Communication (MilSatCom) series of satellites are proposed to measure root-zone soil moisture through heavy vegetation by recording reflected signals using a simple passive microwave receiver [20], [21], [22]. More recently, P-band signals have been also used to demonstrate remote sensing of snow water equivalent by analysis of the phase change of the reflected signal [23].

There are a host of navigation and communications satellites illuminating multiple regions of the globe all the time. Furthermore, these satellites span a wide range of the microwave spectrum. Hence, each one of these satellites is a potential candidate for doing different Earth science remote sensing. In order to fully leverage the potential of these SoOp transmitters, it is advantageous to develop bistatic scattering models of Earth terrain that describe land interactions with the signals

at different frequencies in the forward direction. In other words, using scattering models, we can (1) explore new measurement techniques and configurations, (2) understand the advantages and limitations of each technique, (3) identify the optimum frequencies and signal properties that could help resolve the surface parameters of interest, and (4) deliver sets of test data for training retrieval algorithms. With these goals in mind, we recently developed a coherent bistatic vegetation scattering model, based on a Monte Carlo simulation, to simulate polarimetric bistatic reflectometry [24]. Indeed, due to the scarcity of available bistatic data, it appears that scattering models are a critical step in advancement of these studies and in the design of future missions or field campaigns.

Despite the somewhat large amount of existing data for soil moisture or vegetation biomass retrieval from monostatic active/passive microwave systems and numerous theoretical models (dating back to the 1970s), bistatic scattering models capable of estimating land parameters from space are still in relatively early stages of development. Very few models which can handle bistatic configurations have so far been developed and can be grouped into two basic categories. The first group [25], [26], [27], [28], [29] is incoherent models that are based on Radiative Transfer (RT) theory. This approach is a heuristic method based on the law of energy conservation, so it supplies no phase information. The second group [30], [24] is coherent models that are based on analytical wave theory in conjunction with the distorted Born approximation and perform coherent sum of the scattered fields. They provide complex field quantities and thus include both amplitude and phase information. This enables one to simulate polarimetric bistatic reflectometry for various polarization combinations and to realize interferometric or beamforming techniques.

In [25], Michigan Microwave Canopy Scattering (MIMICS) model, which is based on the first-order RT theory, is extended to bistatic geometry (hence called Bi-MIMICS). The model has been applied to tree canopies at X, C, and L-bands with linear polarizations. The bistatic scattering results are compared with those in the backscatter direction to find out optimum sensing configuration for forest biomass estimation. Wu and Jin [29] modified Bi-MIMIC model by including combination of circular and linear polarizations of transmit/receiver to investigate the effect of various observation angles and polarization combinations on the bistatic reflectometry over Aspen stands.

In [26], an RT-based multiple-scattering model (called Tor Vergeta), which is intrinsically bistatic, is extended to consider specular scattering by including circular polarization in forward direction, focusing on GNSS-R applications to biomass monitoring of forests. The model combines the scattering and extinction properties of each scatterer using the Matrix Doubling algorithm. Guerriero *et al.* [27] employed the Tor Vergeta model to perform simulations of the scattering coefficient of corn at linear polarizations, over a wide range of observation angles at L- and C-band. Later, Pierdicca *et al.* [28] developed a simulator (called SAVERS) for GNSS reflections from bare and vegetated soils, which uses the Tor Vergeta model with circular polarization. The polarization synthesis technique, applied to take antenna polarization mismatch and crosstalk into account, has been presented. Preliminary assessment of the simulator is successfully demonstrated against the field data acquired over sunflower plants during a growing cycle.

Thirion-Lefevre *et al.*, [30] studied bistatic scattering by forested areas using a coherent scattering model called COBISMO, which is an extension of previous developed coherent backscatter model.

They considered linear polarization and analyzed radiometric and polarimetric aspects of bistatic scattering coefficients of forest canopies at P-band to check the physical relevance of the model behavior. The present model, SCoBi-Veg, falls in the same category with COBISMO, but includes more comprehensive antenna characteristics as well as circular polarization since the SoOp transmitters are often circularly polarized and the receiver antennas cannot be constructed to produce pure polarization states.

The SCoBi-Veg model calculates the received complex field in three main contributions: (1) direct term, (2) specular term, (3) diffuse term by explicitly accounting for both antenna and scene characteristics. The first contribution represents the line of sight or the shortest path between the antennas while the second term denotes the forward scattering along the specular direction. Lastly, the diffusely scattered waves arrive at the receiver antenna from a wide range of angles in both azimuth and elevation due to scattering from the illuminated volume. An average diffuse term is obtained by a sufficient number of realizations of vegetation through Monte Carlo simulations. In received reflected field, the antenna characteristics and orientation play a key role. For instance, for ground-based systems, the antenna radiation pattern projected on the surface is not uniformly distributed in phase, amplitude, or polarization. The bistatic radar coefficient calculated by the model thus needs to have the antenna characteristics embedded in it as well as the statistical and physical properties of the terrain to mimic the real measurement setting. Previous studies have usually assumed plane wave illumination/scattering, and/or ignored such antenna effects. The SCoBi-Veg model considers variations of both the strength and polarization states of the received wave along the beam direction so that the same model could be uniformly applied across different

platforms at various altitudes. This is an important step since the ground-based receivers are often used for validation of spaceborne instruments.

The present paper aims at presenting an overview of the newly formulated coherent bistatic vegetation model, i.e. SCoBi-Veg, as well as P-band analysis of polarimetric specular and diffuse contributions for a tree canopy. A companion paper is currently in preparation to provide details of open-source implementation of the SCoBi-Veg model in MATLAB/Octave environment. The next section (Section II of the paper) starts providing explicit expressions of direct, specular, and diffuse contributions to the received field in a general bistatic configuration. The field quantities are then converted to the polarimetric received power in modified Stoke vectors. The section concludes with specializing the model for geometries where the relative distance of the transmitter to the receiver with respect to the specular ground point is large. This represents the most common observation configuration for SoOp concepts. Section III first introduces the simulation setting and parameters at P-band, and then provides simulation results and discussion of the results. Finally, section IV summarizes the important aspects of the model and draws conclusions based on the simulated results. Four appendices are provided at the end to supplement understanding of the model formulation, definitions, and notations.

II. MODEL

In this section, the details of the formulation behind the SCoBi-Veg model will be presented. A general bistatic scattering case is first considered, where two antennas do not have their main beam axis pointing at each other and both of which are overlooking the vegetation. One antenna system

is associated with the SoOp transmitter while the other refers to the passive receiver. The vegetation is represented as ensemble of canonical scatterers located above a flat ground. The model calculates direct, specular, and diffuse components of the received complex field for wide-beam antenna system with nonzero-cross-polarization. The model is specialized to the most common SoOp application where, the transmitter is located far away. The local incident angles are assumed to be constant (parallel) and spreading loss effects due to the incoming wave are ignored, but the spreading loss and sphericity of the scattered wave are considered due to proximity of the receiver platforms that may operate close to the ground. This configuration will represent “plane wave incidence” and “spherical wave scattering”. Furthermore, the formulation considers variations of both the strength and polarization states of the received wave along the beam direction by taking into account for the polarization mismatch and crosstalk. Since the model preserves the phase of the scattered field from the canopy, it allows us to calculate various combination of transmit-receive polarization combinations to investigate various polarization signatures.

A. General Case

In this subsection, we will consider a general bistatic scattering case where two antennas do not have their main beam axis pointing at each other. A step-by-step process will be outlined to obtain the received field when two non-ideal antennas are mismatched in polarization. A transmit antenna located at point T (at a height of h_t) is considered to be illuminating the Earth surface and another antenna as a receiver located at point R (at a height of h_r) is collecting the scattered field from the surface as depicted in **Fig. 1**. In this study, the earth surface is assumed to be planar, mostly valid for ground-based or low-altitude aircraft platforms, while the same formulation can be extended

for spaceborne geometries, where the earth curvature is important. In the reference coordinate system (x, y, z) , the zenith (or surface normal $\hat{\mathbf{n}}$) is in $\hat{\mathbf{z}}$ direction while the unit vectors $\hat{\mathbf{x}}$ and $\hat{\mathbf{y}}$ forms the ground ($x - y$ plane) and are aligned with the local east and north directions, respectively. The reference frame defined here is similar to the standard local East, North, Up (ENU) system. The transmit antenna in a coordinate system (x_t, y_t, z_t) points to the ground (point B_t) with the incidence angle $\theta_{0t} = \cos^{-1}(-\hat{\mathbf{n}} \cdot \hat{\mathbf{z}}_t)$ while the receive antenna in a coordinate system (x_r, y_r, z_r) points to the ground (point B_r) with the incidence angle $\theta_{0r} = \cos^{-1}(-\hat{\mathbf{n}} \cdot \hat{\mathbf{z}}_r)$. The main beam (boresight) axis of both antennas are aligned with their own local z coordinates. For notational clarity, unit vectors are bolded with a hat over them while vectors with magnitudes other than one will be bolded only. In addition, the subscript r refers to a quantity associated with the receive antenna, and t is associated with the transmit antenna.

The electric field radiated by an antenna is commonly defined by a spherical coordinate system. The incident wave, having θ_t and φ_t components in transmit antenna frame, travels in the radial direction $\hat{\mathbf{k}}_i$ from the transmitter, while the scattered wave, having θ_r and φ_r components in receive antenna frame, travels in the radial direction $\hat{\mathbf{k}}_o$ towards the receiver. One can write:

$$\hat{\mathbf{k}}_i = \hat{\mathbf{x}}_t \sin \theta_t \cos \varphi_t + \hat{\mathbf{y}}_t \sin \theta_t \sin \varphi_t + \hat{\mathbf{z}}_t \cos \theta_t \quad (1.a)$$

$$-\hat{\mathbf{k}}_o = \hat{\mathbf{x}}_r \sin \theta_r \cos \varphi_r + \hat{\mathbf{y}}_r \sin \theta_r \sin \varphi_r + \hat{\mathbf{z}}_r \cos \theta_r \quad (1.b)$$

where the subscript i refers to a quantity associated with incident (transmitted) wave, and o is associated with the scattered (received) wave. The orthonormal unit vectors $(\hat{\mathbf{x}}_t, \hat{\mathbf{y}}_t, \hat{\mathbf{z}}_t)$ and $(\hat{\mathbf{x}}_r, \hat{\mathbf{y}}_r, \hat{\mathbf{z}}_r)$ are defined along the antenna coordinate axes.

218

219 The point S in **Fig. 1** denotes the location of the point of reflection that follows the shortest
220 multipath distance from ground. This is called the “Specular Point”, where the incident and
221 reflected waves make the same angle of θ_s with the surface normal. It is determined from simple
222 image theory by confining the discussion to a plane earth. Also shown is a local coordinate system
223 (x', y', z') centered at the specular point S . The x' -axis lies along the ground range between the
224 source and the receiver (between projected points G_t and G_r) while the z' -axis is normal to the
225 surface. The angle between the local x' -axis and the reference x -axis, $\varphi = \cos^{-1}(\hat{\mathbf{x}} \cdot \hat{\mathbf{x}}')$, defines
226 the azimuth direction of the transmit antenna from the local east. The orthonormal unit vectors
227 $(\hat{\mathbf{x}}', \hat{\mathbf{y}}', \hat{\mathbf{z}}')$ are defined along the local coordinate axes.

228

229 In reality, the energy source illuminates a large region of the surface, depending on the extent of
230 the transmit antenna main beam. Radiation traveling from surface points by any other path than
231 the specular point will travel a longer distance. The difference between any other path length and
232 the shortest distance will form a family of ellipses on the ground. The elliptic zones can be defined
233 around the specular point with unique phase differences (multiples of half-wavelengths) called
234 Fresnel zones. The exact dimensions of the Fresnel ellipses are given in [31] for planar Earth.
235 Depending on the surface roughness and vegetation, the number of contributing zones may differ.
236 In addition, the beam-limited configuration (i.e., the footprints of both the transmit and receive
237 antennas) or pulse-limited signals constrain the zones.

238

239 Let us now situate some vegetation over the ground plane. In **Fig. 2**, bistatic scattering over a
240 vegetated landscape is illustrated from a perspective (looking along y') that is perpendicular to the

plane containing the receiver, transmitter, and specular points. The canopy is represented as an ensemble of canonical scatterers located above the ground plane. This approach is called “discrete scatterer” where the canopy can consist of randomly distributed branches, stems, leaves, needles, and vertically distributed tree trunks or stalks all having prescribed location and orientation statistics. Branches, trunks, and stalks are modeled as finitely long lossy-dielectric cylinders [32], [33] and leaves are modelled as flat thin dielectric discs [34], [35]. The single-scattering characteristics of these constituents when averaged determine the attenuation and scattering properties of the canopy. The advantage of the discrete approach is that the results are expressed in terms of quantities (plant geometry and orientation statistics) that are related to the biophysical properties of individual plants. These canonical scatterers are assumed to be uniformly distributed throughout the layer.

For sake of convenience, the local coordinate system (x', y', z') is moved to the top surface of the vegetation. The ground ($z = 0$) is thus represented by $z' = -d$ plane in local coordinates. The transmit and receive antennas are located at \mathbf{x}_i and \mathbf{x}_o , respectively. The total received field will have direct and multipath components:

$$\underline{b} = \begin{bmatrix} b_1 \\ b_2 \end{bmatrix} = \underline{b}_d + \underline{b}_m \quad (2.a)$$

where the direct component is

$$\underline{b}_d = \begin{bmatrix} b_{1d} \\ b_{2d} \end{bmatrix} \quad (2.b)$$

261 and the multipath component is

$$\underline{b}_m = \begin{bmatrix} b_{1m} \\ b_{2m} \end{bmatrix} \quad (2.c)$$

262

263 The elements of \underline{b} vector (i.e., b_1 and b_2) represent network scattering parameters at the physical
264 antenna ports such as port 1 (along x_r -axis) and port 2 (along y_r -axis), respectively, when the
265 antenna is in reception mode. They are complex voltage quantities and their magnitude squares
266 are equal to received power at each port [36]. Throughout the text, the lowercase letters with a
267 single underline denote two-by-one vectors while two-by-two matrices are likewise indicated
268 using lowercase letters with a double underline.

269

270 The multipath component will have coherent (specular reflection) and incoherent (off-specular
271 scattering) contributions:

$$\underline{b}_m = \underline{b}_m^{coh} + \underline{b}_m^{inc} \quad (3.a)$$

272

273 where the incoherent contribution is

$$\underline{b}_m^{inc} = \begin{bmatrix} b_{1m}^{inc} \\ b_{2m}^{inc} \end{bmatrix} \quad (3.b)$$

274 and the coherent contribution is

$$\underline{b}_m^{coh} = \begin{bmatrix} b_{1m}^{coh} \\ b_{2m}^{coh} \end{bmatrix} \quad (3.c)$$

275

276 Below, each contribution will be described separately:

277

1. Direct Contribution:

This contribution represents the shortest path where the transmitted signal arrives at the receiving antenna directly and is given by:

$$\underline{b}_d(\hat{\mathbf{k}}_d) = K \frac{e^{ik_0 r_d}}{r_d} \underline{g}_r(\hat{\mathbf{k}}_d) \cdot \underline{u}_{t \rightarrow r}(\hat{\mathbf{k}}_d) \cdot \underline{g}_t(\hat{\mathbf{k}}_d) \cdot \underline{e}_t \quad (4.a)$$

where $\hat{\mathbf{k}}_d$ is the unit vector from the transmit antenna to the receiver antenna and the constant K is given by

$$K = i \frac{\lambda}{4\pi} \sqrt{G_{0r} EIRP} \quad (4.b)$$

where $i = \sqrt{-1}$ is the unit complex number, $EIRP = P_t G_{0t}$ is equivalent isotropic radiated power (EIRP), λ is wavelength in free space, P_t is power transmitted, G_{0t} is the maximum gain of the transmit antenna, G_{0r} is the maximum gain of the receive antenna, and r_d is the slant range - the distance between the transmit and receive antennas, k_0 is the free-space wavenumber i.e., $k_0 = 2\pi f_0/c$, with f_0 being the frequency and c being the speed of propagation in free space.

It is important to realize that antennas cannot be constructed to produce pure polarization states [37]. There will always be some nonzero cross polarization level (crosstalk isolation). Nevertheless, we refer to the antenna, for example, as linearly polarized. Here it is recognized that we mean “nominally” linear (horizontal), and a cross-polarized (vertical) component will be present. Similarly, for a circularly polarized antenna, we mean “nominally” right-hand circularly

polarized (RHCP), and a cross-polarized (left-hand circularly polarized - LHCP) component will be present. As discussed in **Appendix A**, the pattern matrices can be constructed to take into account the cross-polarization leakage between ports of the antennas. In **Eq. (4.a)**, the receive and transmit antenna patterns are represented by the two by two matrices $\underline{\underline{g}}_r$ and $\underline{\underline{g}}_t$, called normalized “voltage” pattern matrices, respectively. Their expressions are given in **Eqs. (A.3) and (A.6)** for linearly and circularly polarized antennas, respectively.

The vector $\underline{e}_t = [e_1 \ e_2]^T$ in **Eq. (4.a)** defines the nominal polarization state of the transmit antenna ports and its magnitude is equal to one. It represents the polarization state in the main beam direction of the transmit antenna. The polarization, however, varies for increased off-axis angles over the radiation pattern. Due to the orientation of the transmit and the receive antennas, the antenna polarization states are different off the boresight and this will introduce polarization mismatch (or loss). One can relate polarization states of the transmit and receive antennas through a polarization (field) rotation matrix (See **Appendix B**). For instance, the rotation matrix from circularly-polarized transmit antenna basis $(\hat{\mathbf{u}}_{t1}^R, \hat{\mathbf{u}}_{t2}^L)$ to linearly polarized receive antenna basis $(\hat{\mathbf{u}}_{r1}^X, \hat{\mathbf{u}}_{r2}^Y)$ can be written as :

$$\underline{\underline{u}}_{t \rightarrow r}(\hat{\mathbf{k}}_d) = \begin{bmatrix} \hat{\mathbf{u}}_{t1}^R \cdot \hat{\mathbf{u}}_{r1}^{X*} & \hat{\mathbf{u}}_{t2}^L \cdot \hat{\mathbf{u}}_{r1}^{X*} \\ \hat{\mathbf{u}}_{t1}^R \cdot \hat{\mathbf{u}}_{r2}^{Y*} & \hat{\mathbf{u}}_{t2}^L \cdot \hat{\mathbf{u}}_{r2}^{Y*} \end{bmatrix} \quad (4.c)$$

where the symbol $*$ represents complex conjugate, the superscripts R , L , X , and Y denote RHCP, LHCP, linear polarization in X direction (along x -axis port), and linear polarization in Y direction (along y -axis port), respectively, as defined in **Appendix A**. In this study, the antenna y -axis of

both transmit and receive frames is chosen to always be parallel to the ground, so that it represents the horizontal polarized port while the other port (x -axis) represent vertical polarization when the antenna is linearly polarized. This scheme is accomplished through antenna rotation matrices as described in **Appendix C**.

2. *Specular Reflection (Coherent) Contribution:*

The coherent contribution represents the reflection from the specular point S on the ground. According to image theory under the assumption that the surface is of infinite extent, it can be written as

$$\underline{b}_r^{coh} = K \frac{e^{ik_0(r_{st}+r_{sr})}}{(r_{st} + r_{sr})} \underline{\underline{g}}_r(\hat{\mathbf{o}}_s^+) \cdot \underline{\underline{u}}_{s \rightarrow r}(\hat{\mathbf{o}}_s^+) \cdot \underline{\underline{r}}_s(\hat{\mathbf{o}}_s^+, \hat{\mathbf{i}}_s^-) \cdot \underline{\underline{u}}_{t \rightarrow s}(\hat{\mathbf{i}}_s^-) \cdot \underline{\underline{g}}_t(\hat{\mathbf{i}}_s^-) \cdot \underline{e}_t \quad (5.a)$$

where the constant K is defined above in **Eq. (4.b)**, the distances r_{st} and r_{sr} are the ranges from the transmit antenna to the specular point and from the receive antenna to the specular point, respectively.

The wave attenuates as it propagates down from the top of the vegetation to the ground. It then reflects from the surface specularly and it again attenuates from the ground to the top of the vegetation. The coherent term is essentially attenuated twice by the vegetation. The attenuation and phase change of the coherent wave, propagating in the equivalent medium, is found by calculating the mean field within the medium [38]. This process can be written as a specular reflection matrix:

341

$$\underline{\underline{r}}_s(\hat{\mathbf{o}}_s^+, \hat{\mathbf{i}}_s^-) = \underline{\underline{t}}(\hat{\mathbf{o}}_s^+) \cdot \underline{\underline{r}}_g(\theta_s) \cdot \underline{\underline{t}}(\hat{\mathbf{i}}_s^-) \quad (6)$$

342

343 where $\underline{\underline{t}}$ is the vegetation transmission matrix and $\underline{\underline{r}}_g$ is the ground reflection matrix. The unit
 344 vectors, $\hat{\mathbf{i}}_s^-$ and $\hat{\mathbf{o}}_s^+$ describe the wave propagation in the incoming and outgoing directions,
 345 respectively. The superscripts + and - are used to denote the wave modes propagating in the
 346 positive and negative z direction. The subscript s indicates that quantities are calculated for the
 347 specular point. The angle θ_s is the angle of reflection at the specular point and can be calculated
 348 as:

$$\theta_s = \cos^{-1}\{-\hat{\mathbf{n}} \cdot \hat{\mathbf{i}}_s^-\} = \cos^{-1}\{\hat{\mathbf{n}} \cdot \hat{\mathbf{o}}_s^+\} \quad (7)$$

349

350 The transmission matrix is responsible for the incident and scattered waves to experience
 351 attenuation when they travel in the mean medium [39]. Under the assumption that the scatterers
 352 are uniformly distributed in azimuth, the following expression for the one-way transmission matrix
 353 is obtained:

$$\underline{\underline{t}}(\hat{\mathbf{i}}) = \begin{bmatrix} e^{i\Delta\kappa_{zp}(\hat{\mathbf{i}})d} & 0 \\ 0 & e^{i\Delta\kappa_{zq}(\hat{\mathbf{i}})d} \end{bmatrix} \quad (8.a)$$

354

355 where d is the depth of the vegetation, $\hat{\mathbf{i}}$ is a unit vector in the direction of propagation (i.e., $\hat{\mathbf{i}}_s^-$ or
 356 $\hat{\mathbf{o}}_s^+$), and the exponents of matrix elements are of the form (Foldy–Lax approximation) [40], [41]:

357

$$\Delta\kappa_{eq}(\hat{\mathbf{i}}) = \frac{2\pi}{k_0 \cos \theta} \sum_{\alpha} \rho_{\alpha} \overline{f_{qq}^{\alpha}}(\hat{\mathbf{i}}, \hat{\mathbf{i}}; \beta_{\alpha}) \quad (8.b)$$

358

where the angle θ is the angle between the unit vector $\hat{\mathbf{i}}$ and z-axis. The summation index α denotes the scatterer types such as leaves, needles, branches, stalks, or trunks, etc. The number density of the scatterer type α is given by ρ_α . Here, the quantity $f_{pq}^\alpha(\hat{\mathbf{o}}; \hat{\mathbf{i}}; \beta_\alpha)$ denotes the bistatic scattering amplitude of the scatterer type α , where $\hat{\mathbf{i}}$ is in the direction of the incident wave and $\hat{\mathbf{o}}$ is in the direction of the observation point. The subscripts p and q can be horizontal (H) or vertical (V), and as a result, co- and cross-polarized cases are treated simultaneously.

The quantity β_α describes the orientation, size, and position statistics of the scatterer type. The bar over the scattering amplitude denotes ensemble average over the angular and size statistics of the particles. The leaves (or needles) are represented by an average-size circular disk (or circular finite cylinder); hence, the averaging is done for orientation angles only. The trunks (or stalks) are vertical and have a typical size. No averaging is therefore performed on trunks (or stalks). The branches (if different kinds are included) can be divided into several groups, and each group can have an average length and an average diameter. Orientation averaging can then be performed on each branch group. Notice that in this formula, $\overline{f_{pq}^\alpha}(\hat{\mathbf{i}}, \hat{\mathbf{i}}; \beta_\alpha)$ is the forward scattering amplitude of the α th group of scatterers.

In **Eq. (6)**, the ground reflection matrix is given by:

$$\underline{\underline{r}}_g(\theta_s) = \begin{bmatrix} \Gamma_{gp}(\theta_s) & 0 \\ 0 & \Gamma_{gq}(\theta_s) \end{bmatrix} \quad (9.a)$$

It is assumed that the rough surface under the vegetation follows Kirchhoff's approximation and has a Gaussian height distribution [42]; therefore, the reflection coefficient of the rough surface is expressed as

$$\Gamma_{gq}(\theta_s) = r_{gq} e^{-2(k_0 s \cos \theta_s)^2} \quad (9.b)$$

where r_{gq} is the q -polarized Fresnel reflection coefficient of the average dielectric surface, s is the surface *rms* height, and θ_s is the angle of reflection from the surface, defined in **Eq. (7)**.

The polarization basis of the receive antenna and the specular ground point along scattered wave ($\hat{\mathbf{o}}_s^+$), denoted by the subscript $s \rightarrow r$, are related by a rotation matrix (see **Appendix B**) that is given by:

$$\underline{\underline{u}}_{s \rightarrow r}(\hat{\mathbf{o}}_s^+) = \begin{bmatrix} \hat{\mathbf{v}}_o^s \cdot \hat{\mathbf{u}}_{r1}^* & \hat{\mathbf{h}}_o^s \cdot \hat{\mathbf{u}}_{r1}^* \\ \hat{\mathbf{v}}_o^s \cdot \hat{\mathbf{u}}_{r2}^* & \hat{\mathbf{h}}_o^s \cdot \hat{\mathbf{u}}_{r2}^* \end{bmatrix} \quad (10.a)$$

where the local horizontal and vertical polarization in the direction from the specular point to the receiver are, respectively, given by

$$\hat{\mathbf{h}}_o^s = \frac{\hat{\mathbf{n}} \times \hat{\mathbf{o}}_s^+}{|\hat{\mathbf{n}} \times \hat{\mathbf{o}}_s^+|} \quad \text{and} \quad \hat{\mathbf{v}}_o^s = \hat{\mathbf{h}}_o^s \times \hat{\mathbf{o}}_s^+ \quad (10.b)$$

where $\hat{\mathbf{n}} = \hat{\mathbf{z}}'$ and the horizontal polarization vector $\hat{\mathbf{h}}_o^s$ is parallel to the local $x' - y'$ plane.

The polarization basis of the transmit antenna and the specular point along the incident wave ($\hat{\mathbf{i}}_s^-$), denoted by the subscript $t \rightarrow s$, are related by a rotation matrix (see **Appendix B**) that is given by:

$$\underline{\underline{u}}_{t \rightarrow s}(\hat{\mathbf{i}}_s^-) = \begin{bmatrix} \hat{\mathbf{u}}_{t1} \cdot \hat{\mathbf{v}}_i^{s*} & \hat{\mathbf{u}}_{t2} \cdot \hat{\mathbf{v}}_i^{s*} \\ \hat{\mathbf{u}}_{t1} \cdot \hat{\mathbf{h}}_i^{s*} & \hat{\mathbf{u}}_{t2} \cdot \hat{\mathbf{h}}_i^{s*} \end{bmatrix} \quad (11.a)$$

where the local horizontal and vertical polarization in the direction from transmitter to the specular point are respectively given by

$$\hat{\mathbf{h}}_i^s = \frac{\hat{\mathbf{i}}_s^- \times \hat{\mathbf{n}}}{|\hat{\mathbf{i}}_s^- \times \hat{\mathbf{n}}|} \quad \text{and} \quad \hat{\mathbf{v}}_i^s = \hat{\mathbf{i}}_s^- \times \hat{\mathbf{h}}_i^s \quad (11.b)$$

where the horizontal polarization vector $\hat{\mathbf{h}}_i^s$ vector is parallel to local $x' - y'$ plane.

3. Diffuse Scattering (Incoherent) Contribution:

The diffusely scattered waves arrive at the receiver antenna from a wide range of angles in both azimuth and elevations due to scattering from the illuminated volume within the contributing Fresnel zones. In “discrete scatterer” modeling [39], [43], the vegetation layer is usually replaced by a slab of equivalent homogenous medium by the Foldy-Lax theory. Using analytical wave theory in conjunction with distorted Born approximation [39], the transmit and receive antenna effects (i.e., polarization, orientation, shape, etc.) can be explicitly accounted for.

Let us consider the geometry of the problem, pictured in **Fig. 3**, where a single scatterer of type α is embedded at point P_α in the medium over the half-space. The position vector is given by $\mathbf{r}_\alpha = x_\alpha \hat{\mathbf{x}}' + y_\alpha \hat{\mathbf{y}}' - z_\alpha \hat{\mathbf{z}}'$ in local coordinates. An expression for the received field due to this single particle was obtained by employing distorted Born approximation in [44] with the assumption that the regular far-field conditions hold, i.e., each scatterer in the vegetation layer is in the far-zone of the transmit antenna and the receive antenna is also in the far-zone of each scatterer within the layer. Additionally, the antennas with narrow beam and pure polarization state were considered.

The results in [44] are here adapted to a general case where both antennas are considered to be wide-beam with nonzero-cross-polarized components. This implies that the strength and polarization of the transmitted and received wave depend on the antenna properties along the beam direction. Summing the result of the single particle scattering over all types and particles, and taking into account the polarization mismatch (rotation matrices) and the polarization crosstalk (antenna pattern matrices with co- and cross-pol components) leads to the following:

$$\underline{b}_r^{inc} = K \frac{e^{ik_0(r_{st}+r_{sr})}}{r_{st}r_{sr}} \sum_{\alpha} \sum_{n=1}^{N_{\alpha}} \sum_x B_{\alpha,n}^x \left[\underline{g}_r(\hat{\mathbf{o}}_x) \cdot \underline{u}_{p \rightarrow r}(\hat{\mathbf{o}}_x) \cdot \underline{s}_{\alpha,n}^x(\hat{\mathbf{o}}_x, \hat{\mathbf{i}}_x) \cdot \underline{u}_{t \rightarrow p}(\hat{\mathbf{i}}_x) \cdot \underline{g}_t(\hat{\mathbf{i}}_x) \cdot \underline{e}_t \right] \quad (12)$$

where the constant K and the distances r_{st} and r_{sr} are defined above, and N_{α} is the number of particle of type α within the illuminated volume around the specular point. The normalized “voltage” pattern matrices, \underline{g}_t and \underline{g}_r , of transmit and receive antennas are given in **Appendix A** and can be linearly or circularly polarized as discussed earlier. The strengths of the incident and

435 scattered waves at each particle are directly proportional to the value of the antenna patterns along
 436 that direction.

437

438 The wave from each particle follows four distinct paths before arriving at the receiver, denoted by
 439 $x \in \{dd, rd, dr, rr\}$. Each mechanism is described by the following scattering matrices

440

$$\underline{\underline{S}}_{\alpha,n}^{dd}(\hat{\mathbf{o}}_{\alpha}^{+}, \hat{\mathbf{i}}_{\alpha}^{-}) = \underline{\underline{t}}(\hat{\mathbf{o}}_{\alpha}^{+}) \cdot \underline{\underline{f}}_{\alpha}(\hat{\mathbf{o}}_{\alpha}^{+}, \hat{\mathbf{i}}_{\alpha}^{-}; \beta_{\alpha,n}) \cdot \underline{\underline{t}}(\hat{\mathbf{i}}_{\alpha}^{-}) \quad (13.a)$$

$$\underline{\underline{S}}_{\alpha,n}^{dr}(\hat{\mathbf{o}}_{\alpha}^{+}, \hat{\mathbf{i}}_{\alpha l}^{+}) = \underline{\underline{t}}(\hat{\mathbf{o}}_{\alpha}^{+}) \cdot \underline{\underline{f}}_{\alpha}(\hat{\mathbf{o}}_{\alpha}^{+}, \hat{\mathbf{i}}_{\alpha l}^{+}; \beta_{\alpha,n}) \cdot \underline{\underline{r}}_g(\hat{\mathbf{i}}_{\alpha l}^{+}) \cdot \underline{\underline{t}}(\hat{\mathbf{i}}_{\alpha l}^{+}) \quad (13.b)$$

$$\underline{\underline{S}}_{\alpha,n}^{rd}(\hat{\mathbf{o}}_{\alpha l}^{-}, \hat{\mathbf{i}}_{\alpha}^{-}) = \underline{\underline{t}}(\hat{\mathbf{o}}_{\alpha l}^{-}) \cdot \underline{\underline{r}}_g(\hat{\mathbf{o}}_{\alpha l}^{-}) \cdot \underline{\underline{f}}_{\alpha}(\hat{\mathbf{o}}_{\alpha l}^{-}, \hat{\mathbf{i}}_{\alpha}^{-}; \beta_{\alpha,n}) \cdot \underline{\underline{t}}(\hat{\mathbf{i}}_{\alpha}^{-}) \quad (13.c)$$

$$\underline{\underline{S}}_{\alpha,n}^{rr}(\hat{\mathbf{o}}_{\alpha l}^{-}, \hat{\mathbf{i}}_{\alpha l}^{+}) = \underline{\underline{t}}(\hat{\mathbf{o}}_{\alpha l}^{-}) \cdot \underline{\underline{r}}_g(\hat{\mathbf{o}}_{\alpha l}^{-}) \cdot \underline{\underline{f}}_{\alpha}(\hat{\mathbf{o}}_{\alpha l}^{-}, \hat{\mathbf{i}}_{\alpha l}^{+}; \beta_{\alpha,n}) \cdot \underline{\underline{r}}_g(\hat{\mathbf{i}}_{\alpha l}^{+}) \cdot \underline{\underline{t}}(\hat{\mathbf{i}}_{\alpha l}^{+}) \quad (13.d)$$

441

442 where the unit vectors are defined as

$$\hat{\mathbf{i}}_{\alpha}^{-} = \frac{\mathbf{r}_i}{r_i}, \quad r_i = |\mathbf{r}_i| = |\mathbf{r}_{\alpha} - \mathbf{x}_i| \quad (14.a)$$

$$\hat{\mathbf{o}}_{\alpha}^{+} = \frac{\mathbf{r}_o}{r_o}, \quad r_o = |\mathbf{r}_o| = |\mathbf{r}_{\alpha} - \mathbf{x}_o| \quad (14.b)$$

$$\hat{\mathbf{i}}_{\alpha l}^{+} = \frac{\mathbf{r}_{il}}{r_{il}}, \quad r_{il} = |\mathbf{r}_{il}| = |\mathbf{r}_{\alpha} - \mathbf{x}_{il}| \quad (14.c)$$

$$\hat{\mathbf{o}}_{\alpha l}^{-} = \frac{\mathbf{r}_{ol}}{r_{ol}}, \quad r_{ol} = |\mathbf{r}_{ol}| = |\mathbf{r}_{\alpha} - \mathbf{x}_{ol}| \quad (14.d)$$

443

444 and where the superscripts + and - are used to denote the wave modes propagating in the positive
 445 and negative z direction, respectively. The subscript l is introduced in the notation to refer to the
 446 auxiliary image antenna.

Fig. 4 illustrates the scattering mechanisms for a single particle. The reflected paths are illustrated by the image antenna representation, where the images of the transmit and receive antennas with respect to ground are positioned at $\mathbf{x}_{iI} = \mathbf{x}_i - 2(\mathbf{x}_i \cdot \hat{\mathbf{z}}' + d)\hat{\mathbf{z}}'$ and $\mathbf{x}_{oI} = \mathbf{x}_o - 2(\mathbf{x}_o \cdot \hat{\mathbf{z}}' + d)\hat{\mathbf{z}}'$, respectively. In order to account for the attenuation of the reflected components, an image medium is included in the figure. Each scattering mechanism can be visualized as follows.

- Single Bounce Contribution: Direct-direct (dd) term follows the path $\mathbf{T}\mathbf{P}_\alpha\mathbf{R}$. The field travels in the direction of $\hat{\mathbf{i}}_x = \hat{\mathbf{i}}_\alpha^-$ towards the particle of type α , located at \mathbf{r}_α , and then the incident field is bistatically scattered from this particle and travels in the direction of $\hat{\mathbf{o}}_x = \hat{\mathbf{o}}_\alpha^+$ towards the receive antenna.
- Double Bounce Contributions: It includes two mechanisms such as reflected-direct (dr) and direct-reflected (rd) terms. The first mechanism follows the path $\mathbf{T}_I\mathbf{P}_\alpha\mathbf{R}$. The field incident on the particle in the direction of $\hat{\mathbf{i}}_x = \hat{\mathbf{i}}_{\alpha I}^+$ from the image of the transmit antenna is reflected from the ground and bistatically scattered from the particle in the direction of $\hat{\mathbf{o}}_x = \hat{\mathbf{o}}_\alpha^+$ towards the receive antenna. The second mechanism follows the path $\mathbf{T}\mathbf{P}_\alpha\mathbf{R}_I$. The field incident on the particle in the direction of $\hat{\mathbf{i}}_x = \hat{\mathbf{i}}_\alpha^-$ is bistatically scattered from the particle in the direction of $\hat{\mathbf{o}}_x = \hat{\mathbf{o}}_{\alpha I}^-$ towards the image of receive antenna after reflection from the ground.
- Triple Bounce Contribution: Reflected-reflected (rr) term follows the path $\mathbf{T}_I\mathbf{P}_\alpha\mathbf{R}_I$. The field incident on the particle in the direction of $\hat{\mathbf{i}}_x = \hat{\mathbf{i}}_{\alpha I}^+$ from the image of the transmit antenna is reflected from the ground and bistatically scattered from the particle in the

direction of $\hat{\mathbf{o}}_x = \hat{\mathbf{o}}_{\alpha l}^-$ towards the image of receive antenna after reflection from the ground. It involves double reflection from the ground.

The bistatic scattering from the particle of type α is described by a bistatic scattering amplitude matrix $\underline{\underline{f}}_\alpha(\hat{\mathbf{o}}_x, \hat{\mathbf{i}}_x; \beta_{\alpha, n})$ as:

$$\underline{\underline{f}}_\alpha(\hat{\mathbf{o}}_x, \hat{\mathbf{i}}_x; \beta_{\alpha, n}) = \begin{bmatrix} f_{VV}^\alpha(\hat{\mathbf{o}}_x, \hat{\mathbf{i}}_x; \beta_{\alpha, n}) & f_{VH}^\alpha(\hat{\mathbf{o}}_x, \hat{\mathbf{i}}_x; \beta_{\alpha, n}) \\ f_{HV}^\alpha(\hat{\mathbf{o}}_x, \hat{\mathbf{i}}_x; \beta_{\alpha, n}) & f_{HH}^\alpha(\hat{\mathbf{o}}_x, \hat{\mathbf{i}}_x; \beta_{\alpha, n}) \end{bmatrix} \quad (15)$$

where the bistatic amplitude $f_{pq}^\alpha(\hat{\mathbf{o}}_x, \hat{\mathbf{i}}_x; \beta_{\alpha, n})$ is defined above. The quantities p and q denote the local polarization states along incident ($\hat{\mathbf{i}}_x$) and scattering ($\hat{\mathbf{o}}_x$) directions, respectively, and can be horizontal (H) or vertical (V). As stated above, the quantity $\beta_{\alpha, n}$ describes the orientation, size, and position statistics of the scatterer type. Note that the polarization of scattering amplitude is given in terms of linear polarization since polarization in the local ground frame is defined with linear polarization basis only.

The ground reflection matrix $\underline{\underline{r}}_g$ is defined in **Eq. (9)** and the transmission matrix $\underline{\underline{t}}$ for the particle located \mathbf{r}_α is given by:

$$\underline{\underline{t}}(\hat{\mathbf{i}}) = \begin{bmatrix} e^{i\Delta\kappa_{zpp}(\hat{\mathbf{i}})r_{z\alpha}(\hat{\mathbf{i}})} & 0 \\ 0 & e^{i\Delta\kappa_{zqq}(\hat{\mathbf{i}})r_{z\alpha}(\hat{\mathbf{i}})} \end{bmatrix} \quad (16)$$

where $\Delta\kappa_{zpp}(\hat{\mathbf{i}})$ is defined in **Eq. (8.b)** and $r_{z\alpha} = |\mathbf{r}_\alpha \cdot \hat{\mathbf{n}}|$ is the vertical distance that the wave propagates within the mean medium. For direct paths from and to the particle (antennas in the real positions), they are given by $r_{z\alpha}(\hat{\mathbf{i}}_\alpha^-) = r_{z\alpha}(\hat{\mathbf{o}}_\alpha^+) = z_\alpha$, while for reflected paths from and to the

particle (antennas in the image positions), they are given by $r_{z\alpha}(\hat{\mathbf{t}}_{\alpha I}^+) = r_{z\alpha}(\hat{\mathbf{o}}_{\alpha I}^-) = -z_\alpha + 2d$.

Since each scattering mechanism follows a different path, the total path traveled will be different.

The factors $B_{\alpha,n}^x$ that account for the spreading loss and path-dependent phase terms for each

mechanism are thus unique and given by:

$$B_{\alpha,n}^{dd} = \left(\frac{e^{ik_0(r_i+r_o)}}{r_i r_o} \right) / \left(\frac{e^{ik_0(r_{st}+r_{sr})}}{r_{st} r_{sr}} \right) \quad (17.a)$$

$$B_{\alpha,n}^{dr} = \left(\frac{e^{ik_0(r_{il}+r_o)}}{r_{il} r_o} \right) / \left(\frac{e^{ik_0(r_{st}+r_{sr})}}{r_{st} r_{sr}} \right) \quad (17.b)$$

$$B_{\alpha,n}^{rd} = \left(\frac{e^{ik_0(r_i+r_{ol})}}{r_i r_{ol}} \right) / \left(\frac{e^{ik_0(r_{st}+r_{sr})}}{r_{st} r_{sr}} \right) \quad (17.c)$$

$$B_{\alpha,n}^{rr} = \left(\frac{e^{ik_0(r_{il}+r_{ol})}}{r_{il} r_{ol}} \right) / \left(\frac{e^{ik_0(r_{st}+r_{sr})}}{r_{st} r_{sr}} \right) \quad (17.d)$$

Fig. 5 illustrates the directions of incoming and outgoing waves at an individual particle (i.e., a

vertical trunk). The polarization basis vectors, defined at the particle, differ for each direction due

to the beam divergence. As a result, four distinct polarization rotation matrices have to be

constructed. Following the procedure in **Appendix B**, the rotation matrices from the particle to

the receiver (denoted by the subscript $p \rightarrow r$) are obtained as

$$\underline{\underline{u}}_{p \rightarrow r}(\hat{\mathbf{o}}_\alpha^+) = \begin{bmatrix} \hat{\mathbf{v}}_\alpha^+ \cdot \hat{\mathbf{u}}_{r1}^* & \hat{\mathbf{h}}_\alpha^+ \cdot \hat{\mathbf{u}}_{r1}^* \\ \hat{\mathbf{v}}_\alpha^+ \cdot \hat{\mathbf{u}}_{r2}^* & \hat{\mathbf{h}}_\alpha^+ \cdot \hat{\mathbf{u}}_{r2}^* \end{bmatrix} \text{ for } x = dd, dr \quad (18.a)$$

$$\underline{\underline{u}}_{p \rightarrow r}(\hat{\mathbf{o}}_{\alpha I}^-) = \begin{bmatrix} \hat{\mathbf{v}}_{\alpha I}^- \cdot \hat{\mathbf{u}}_{r1}^* & \hat{\mathbf{h}}_{\alpha I}^- \cdot \hat{\mathbf{u}}_{r1}^* \\ \hat{\mathbf{v}}_{\alpha I}^- \cdot \hat{\mathbf{u}}_{r2}^* & \hat{\mathbf{h}}_{\alpha I}^- \cdot \hat{\mathbf{u}}_{r2}^* \end{bmatrix} \text{ for } x = rd, rr \quad (18.b)$$

501 and the rotation matrices from the transmitter to the particle (denoted by the subscript $t \rightarrow p$) are
 502 obtained as

$$\underline{\underline{u}}_{t \rightarrow p}(\hat{\mathbf{i}}_{\alpha}^{-}) = \begin{bmatrix} \hat{\mathbf{u}}_{t1} \cdot \hat{\mathbf{v}}_i^{-*} & \hat{\mathbf{u}}_{t2} \cdot \hat{\mathbf{v}}_i^{-*} \\ \hat{\mathbf{u}}_{t1} \cdot \hat{\mathbf{h}}_i^{-*} & \hat{\mathbf{u}}_{t2} \cdot \hat{\mathbf{h}}_i^{-*} \end{bmatrix} \quad \text{for } x = dd, rd \quad (18.c)$$

$$\underline{\underline{u}}_{t \rightarrow p}(\hat{\mathbf{i}}_{\alpha l}^{+}) = \begin{bmatrix} \hat{\mathbf{u}}_{t1} \cdot \hat{\mathbf{v}}_{il}^{+*} & \hat{\mathbf{u}}_{t2} \cdot \hat{\mathbf{v}}_{il}^{+*} \\ \hat{\mathbf{u}}_{t1} \cdot \hat{\mathbf{h}}_{il}^{+*} & \hat{\mathbf{u}}_{t2} \cdot \hat{\mathbf{h}}_{il}^{+*} \end{bmatrix} \quad \text{for } x = dr, rr \quad (18.d)$$

503

504 The local horizontal (parallel to local $x' - y'$ plane) and vertical polarizations for each direction
 505 are given by

$$\hat{\mathbf{h}}_o^{+} = \frac{\hat{\mathbf{n}} \times \hat{\mathbf{o}}_{\alpha}^{+}}{|\hat{\mathbf{n}} \times \hat{\mathbf{o}}_{\alpha}^{+}|} \quad \text{and} \quad \hat{\mathbf{v}}_o^{+} = \hat{\mathbf{h}}_o^{+} \times \hat{\mathbf{o}}_{\alpha}^{+} \quad (19.a)$$

$$\hat{\mathbf{h}}_{oI}^{-} = \frac{\hat{\mathbf{n}} \times \hat{\mathbf{o}}_{\alpha l}^{-}}{|\hat{\mathbf{n}} \times \hat{\mathbf{o}}_{\alpha l}^{-}|} \quad \text{and} \quad \hat{\mathbf{v}}_{oI}^{-} = \hat{\mathbf{h}}_{oI}^{-} \times \hat{\mathbf{o}}_{\alpha}^{+} \quad (19.b)$$

$$\hat{\mathbf{h}}_i^{-} = \frac{\hat{\mathbf{i}}_{\alpha}^{-} \times \hat{\mathbf{n}}}{|\hat{\mathbf{i}}_{\alpha}^{-} \times \hat{\mathbf{n}}|} \quad \text{and} \quad \hat{\mathbf{v}}_i^{-} = \hat{\mathbf{i}}_{\alpha}^{-} \times \hat{\mathbf{h}}_i^{-} \quad (19.c)$$

$$\hat{\mathbf{h}}_{il}^{+} = \frac{\hat{\mathbf{i}}_{\alpha l}^{+} \times \hat{\mathbf{n}}}{|\hat{\mathbf{i}}_{\alpha l}^{+} \times \hat{\mathbf{n}}|} \quad \text{and} \quad \hat{\mathbf{v}}_{il}^{+} = \hat{\mathbf{i}}_{\alpha l}^{+} \times \hat{\mathbf{h}}_{il}^{+} \quad (19.d)$$

506

507 **4. Received Power**

508

509 The total power received can be written in terms of the coherency vector as:

510

$$\underline{\underline{P}}_T = \underline{\underline{b}} \otimes \underline{\underline{b}}^* \quad (20)$$

511

512 where $\underline{\underline{b}}^*$ is conjugate of $\underline{\underline{b}}$ and the operator \otimes indicates an outer product (Kronecker product) that
 513 is defined **in Appendix D**. Under the assumption that the scattering process is stationary and that

the direct and multipath component fields arriving at the antennas from different directions are uncorrelated [45], the total power can be split into three independent terms as:

$$\underline{P}_T = \underline{P}_d + \underline{P}_m^{coh} + \underline{P}_m^{inc} \quad (21.a)$$

where

$$\underline{P}_d = \left\{ \frac{|K|^2}{r_d^2} \right\} \underline{D} \quad (21.b)$$

$$\underline{P}_m^{coh} = \left\{ \frac{|K|^2}{(r_{st} + r_{sr})^2} \right\} \underline{\Gamma}_s \quad (21.c)$$

$$\underline{P}_m^{inc} = \left\{ \frac{|K|^2 A_s}{4\pi r_{st}^2 r_{sr}^2} \right\} \underline{\sigma}_e^0 \quad (21.d)$$

where

$$\underline{D} = \underline{G}_r(\hat{\mathbf{k}}_d) \cdot \underline{U}_{t \rightarrow r}(\hat{\mathbf{k}}_d) \cdot \underline{G}_t(\hat{\mathbf{k}}_d) \cdot \underline{E}_t \quad (22.a)$$

$$\underline{\Gamma}_s = \underline{G}_r(\hat{\mathbf{o}}_s^+) \cdot \underline{U}_{s \rightarrow r}(\hat{\mathbf{o}}_s^+) \cdot \underline{R}_s(\hat{\mathbf{o}}_s^+, \hat{\mathbf{i}}_s^-) \cdot \underline{U}_{t \rightarrow s}(\hat{\mathbf{i}}_s^-) \cdot \underline{G}_t(\hat{\mathbf{i}}_s^-) \cdot \underline{E}_t \quad (22.b)$$

$$\underline{\sigma}_e^0 = \frac{1}{A_s} \sum_{\alpha} \sum_{n=1}^{N_{\alpha}} \sum_x |B_{\alpha,n}^x|^2 \left[\underline{G}_r(\hat{\mathbf{o}}_x) \cdot \underline{U}_{p \rightarrow r}(\hat{\mathbf{o}}_x) \cdot \underline{\sigma}_{\alpha,n}^x(\hat{\mathbf{o}}_x, \hat{\mathbf{i}}_x) \cdot \underline{U}_{t \rightarrow p}(\hat{\mathbf{i}}_x) \cdot \underline{G}_t(\hat{\mathbf{i}}_x) \cdot \underline{E}_t \right] \quad (22.c)$$

where

where four-by-one vectors, such as the coherency vector \underline{P}_T , are written using uppercase letters and a single underline while four-by-four matrices are written using uppercase letters and a double underline. The coherency vectors \underline{D} , $\underline{\Gamma}_s$, and $\underline{\sigma}_e^0$ represent direct signal, specular reflectivity, and “effective” normalized bistatic radar cross section (NBRCS), respectively. Note that antenna effects (e.g., the antenna beamwidths, polarization crosstalk, loss, altitude, etc.) are incorporated into NBRCS (or bistatic scattering coefficient), which should represent the object scattering properties only. The expression in **Eq. (22.c)** is thus called “effective” NBRCS or $\underline{\sigma}_e^0$ and also

indicated with subscript “e”. The effects of system parameters on NBRCS will be examined in the simulation section.

In calculating the outer products, the following identity is utilized $(\underline{\underline{m}} \cdot \underline{\underline{n}}) \otimes (\underline{\underline{m}} \cdot \underline{\underline{n}})^* = (\underline{\underline{m}} \otimes \underline{\underline{m}}^*) \cdot (\underline{\underline{n}} \otimes \underline{\underline{n}}^*)$ and the following vectors/matrices are defined:

The coherency vector of transmit antenna polarization state is given by:

$$\underline{\underline{E}}_t = \underline{\underline{e}}_t \otimes \underline{\underline{e}}_t^* \quad (23)$$

The antenna normalized (power) pattern matrices are given for the receive and transmit antennas, respectively, by:

$$\underline{\underline{G}}_r = \underline{\underline{g}}_r \otimes \underline{\underline{g}}_r^* \quad (24.a)$$

$$\underline{\underline{G}}_t = \underline{\underline{g}}_t \otimes \underline{\underline{g}}_t^* \quad (24.b)$$

The polarization basis rotation matrices that operate on intensities are given by

$$\underline{\underline{U}}_{t \rightarrow r} = \underline{\underline{u}}_{t \rightarrow r} \otimes \underline{\underline{u}}_{t \rightarrow r}^* \quad (25.a)$$

$$\underline{\underline{U}}_{s \rightarrow r} = \underline{\underline{u}}_{s \rightarrow r} \otimes \underline{\underline{u}}_{s \rightarrow r}^* \quad (25.b)$$

$$\underline{\underline{U}}_{t \rightarrow s} = \underline{\underline{u}}_{t \rightarrow s} \otimes \underline{\underline{u}}_{t \rightarrow s}^* \quad (25.c)$$

$$\underline{\underline{U}}_{p \rightarrow r}^x = \underline{\underline{u}}_{p \rightarrow r}^x \otimes \underline{\underline{u}}_{p \rightarrow r}^{x*} \quad (25.d)$$

$$\underline{\underline{U}}_{t \rightarrow p}^x = \underline{\underline{u}}_{t \rightarrow p}^x \otimes \underline{\underline{u}}_{t \rightarrow p}^{x*} \quad (25.e)$$

540 In **Eq. (22.b)**, the specular reflectivity operator that describes the scattering from the specular point
 541 is defined as

$$\underline{\underline{R}}_s = \underline{\underline{r}}_s \otimes \underline{\underline{r}}_s^* \quad (26)$$

542

543 In **Eq. (22.c)**, A_s is the surface area that can be limited to a few Fresnel zones to capture most of
 544 the contributions, and the bistatic scattering cross section operator is given by

545

$$\underline{\underline{\sigma}}_{\alpha,n}^x = 4\pi \left[\underline{\underline{s}}_{\alpha,n}^x \otimes \underline{\underline{s}}_{\alpha,n}^{x*} \right] \quad (27)$$

546 **B. Special Case ($r_{st} \gg r_{sr}$)**

547

548 The expressions given above (namely, **Eq. (21)**) do not impose any restriction on the relative
 549 distance between receiver and transmitter slant ranges except that both transmitter and receiver are
 550 in the far field of each other and both of them are in the far zone of vegetation constituents above
 551 ground. On the other hand, in SoOp studies for remote sensing of Earth properties, the utilized
 552 transmitters are mostly located in medium Earth orbit (MEO) such as GNSS or geostationary orbit
 553 (GEO) such as communication satellites, and the receivers are operated from different platforms:
 554 ground, airborne, or spaceborne at low Earth orbit (LEO). For all of these scenarios, the relative
 555 distance between transmitter and receivers to the specular point is large, i.e., $r_{st} \gg r_{sr}$. By taking
 556 advantage of this large difference, a flat Earth approximation around the specular point can be
 557 applied. Moreover, for the transmitters at MEO and GEO, the range from the transmitter to the
 558 ground and the incidence angle direction can be assumed to be equal for all the surface surrounding

the specular point. The footprint associated with Fresnel zones can be approximated with the following semi-minor and semi-major axes, respectively [46]:

$$b = \frac{\sqrt{2\delta_n h_r \cos \theta_s}}{\cos \theta_s} \quad (28.a)$$

$$a = \frac{b}{\cos \theta_s} \quad (28.b)$$

where θ_s is the angle of reflection at the specular point as defined in **Eq. (7)**, h_r is the receiver height with respect to ground, $\delta_n = n\lambda/2$ is the delay of multiples of half-wavelengths, and n is the Fresnel zone number. Even though one can use the exact expression for Fresnel ellipses given in [31], the above expressions remain fairly accurate for most practical cases [47] and provide a better physical grasp of the footprint. The reflected signal mainly comes within the first ($n = 1$) Fresnel zone over land unless topographic effects are present as indicated by recent studies [3] while the reflected signals over ocean emanate over the multiple Fresnel zones (Glistening zone) [46]. It is important to identify contributing Fresnel zones and the scattering mechanism not only to determine the footprint but also to arrive at a physical model that is suitable for inversion.

The reflected signals are generally a superposition of both the coherent (specular), incoherent (diffuse) scattering, and direct components as given in **Eq. (21)**. For down looking antennas, the direct signal can be significantly suppressed, but the question remains on the relative importance of coherent and incoherent contributions over land with respect to platform altitude. It is important to recognize the path loss dependence with distance of each term. The specularly reflected signal follow a total ray path dependence, i.e. $1/(r_{st} + r_{sr})^2$ due to the image theory while the diffuse

term exhibits a multiplicative dependence given by $1/(r_{st}^2 r_{sr}^2)$ due to the additional spreading loss the incident signal experiences after re-radiation from the vegetation scatterers. The diffuse term thus decreases more rapidly with distance than the specular component. These differences are manifested in the relative weights of the two components for different receiving platforms: ground, airborne, and spaceborne.

Let us assume that specular reflection is dominant over land and find out how much diffuse scattering alters the specular reflectivity as a function of altitude. By normalizing the total power \underline{P}_T with $|K|^2/(r_{st} + r_{sr})^2$, approximating the surface area ($= \pi ab$) with **Eq. (28)**, and neglecting the direct contribution, the reflectivity of the total reflected signal $\underline{\Gamma}_s^{(T)}$ can be obtained:

$$\underline{\Gamma}_s^{(T)} \cong \underline{\Gamma}_s + \left(\frac{\delta_n}{2h_r} \right) \underline{\sigma}_e^0 \quad (29)$$

where the specular reflectivity $\underline{\Gamma}_s$ and the effective NBRCS $\underline{\sigma}_e^0$ are given in **Eq. (22)**. It is evident that the relative contribution of the NBRCS (diffuse contribution) is inversely proportional to the receiver altitude (h_r). This indicates that the specular component contains a greater portion of the total energy and thus contributes more to the received power unless (1) NBRCS is significantly larger than specular reflectivity, (2) more Fresnel zones contribute, (3) the receiver is located at close neighborhood of the ground, or (4) any combination of the above cases happens. Diffuse scattering, although weak at high altitude, can have significant influence on ground and airborne systems which are usually used as a testbed for algorithm development for spaceborne missions. In addition, the reflected signals could still include significant incoherent scattering components and the relative importance of these contributions is expected to vary with respect to the scene

properties around the specular point. For these reasons, the diffuse component should be included in the model for low altitude platforms. A bistatic model based solely on image theory cannot account for diffusely scattering.

III. NUMERICAL RESULTS AND DISCUSSION

The SCoBi-Veg model considers single scattering so it is intrinsically valid at P-, L-, and S-bands. There are already many potential free illuminators within these frequency ranges that could be used for Earth science applications. Furthermore, the model could be extended to exploit signals at other bands if multilayer soil for lower frequencies or multiple scattering for higher frequencies are included. The particular communication satellites of interests to the recent studies [20], [21], [22] are the Navy's Mobile Users Objective System (MUOS) operating with RHCP transmit signals at P-band frequencies (360-380 MHz and 240-270 MHz). There are four MUOS satellites at geostationary altitudes (~32810 km), providing global coverage, except near the polar cap. As a preliminary application of the model, we will limit ourselves to P-band (370 MHz). The purpose of the simulations is two folds: (1) to show physical relevance of the model behavior to the SoOp studies in general and (2) to provide insights into polarimetric aspects of specular and diffuse contributions at P-band for a tree canopy observed from platforms at various altitudes.

The model requires various soil and vegetation parameters as inputs. In this paper, we will use the *in situ* parameters collected in an active/passive soil moisture experiment in Maryland in 2006 [48]. The experimental site consisted of plots of planted stands of deciduous Paulownia trees, a fast-growing deciduous tree with broad leaves shown in **Fig. 8**. The tree plot used in this paper

had 92 trees in a 1089 m² area. The dry biomass was about 9 kg/m², while the woody volume and density were 185.8 m³/ha and 477.6 kg/m³, respectively. The diameter at breast height (DBH) ranged from 17 to 23 cm (average DBH = 19.4 cm). The tree heights were variable, on the order of 11–14 m (average height = 13 m). Detailed measurements of the size/angle distributions of the tree constituents (trunk, branches, and leaves), along with their densities, were made. The results from the canopy sampling and dielectric measurements are shown in **Table I**. Clear boundaries within canopy and trunk layers were identified by visual inspection. The right panel next to the picture in **Fig. 8** shows distribution of vegetation components within the vegetation layers. The soil texture at the site was a loamy sand, consisting of 80% sand and 7% clay. The ground was flat with a relatively smooth surface, where the surface rms height was on the order of 0.5–1 cm.

A. Simulation Setting

The model considers both specular and diffuse scattering by incorporating the statistical and physical properties of the terrain into the received signal. While the calculation of the specular term requires properties of the mean vegetation attenuation in one direction and soil parameters at a single point, the diffuse term involves contributions of various scattering mechanisms due to each particle within the illuminated volume. In this present investigation, a Monte Carlo procedure is chosen to predict the bistatic diffuse response from vegetation. Monte Carlo simulations are very useful to incorporate coherent addition and wave interaction effects in a vegetation canopy. The scheme holds possibility to incorporate realistic canopy structures such as architectural plant model [49], experimental vectorization [38] or recursive Lindenmayer systems [50] due to its generic model formulation. However, the base vegetation module in SCoBi-Veg is restricted for

the moment to use a simple multi-layer canopy model where the scatterers are spread uniformly between illuminated layers using a given distribution. Due to the single scattering assumption, the scatterers are assumed to be independent and no mutual interactions are considered. The scattering contributions of electrically large components only (e.g., primary branches, and trucks at P-band) are considered in order to speed up the computation while the calculation of the mean medium involves attenuation due to all scatterers. The significant scatterers are embedded in the equivalent medium where random positions are generated for these scatterers in the illuminated volume based on their associated layers; each scatterer is then oriented according to some prescribed orientation statistics. The solutions of the bistatic electric fields are computed for each particle by combining the configuration attributes, bistatic scattering amplitude from each significant scatterers, and ground reflection; these are then summed coherently. Finally, by repeating for many realizations of the random medium, the average received field of the bistatic scattered field is obtained from the responses averaged over all realizations.

Over the years, various observing strategies have been developed for SoOp studies, mostly GNSS-R applications. These include (1) standard ground based nearly hemispherical RHCP antenna [10], (2) horizontal-pointing vertically polarized antenna [7], (3) down-looking LHCP antenna and an up-looking RHCP antenna [51], (4) one RHCP up-looking antenna and two down-looking antennas with one RHCP polarized and the other LHCP polarized [9], (5) a two-element dual linearly polarized patch array mounted side of an aircraft by steering a null to the direction of the undesired signal [21]. The model can handle any configuration stated above or more general configuration where vertically and horizontally polarized antennas for both the up and down-looking. In the present investigation, we are however going to restrict the simulations to situation

where the dual circularly polarized receiver antenna (both RHCP and LHCP) points directly to the specular point to understand the angular dependence of polarimetric reflected signatures.

A generalized Gaussian antenna pattern, including 25 dB sidelobes, 25 dB crosstalk and 30° beamwidth (arbitrary values), is assumed as an approximation to the radiation pattern needed in this formulation. This pattern will be assumed to be circularly symmetrical about the direction of peak intensity. In the following simulations, both a receiving antenna gain and EIRP equal to 0 dB were supposed. The actual values depend on the choice of illuminator and actual receiver antenna. They affect the received power in dBm only by an offset and do not change its sensitivity to the reflected signature. Additional processing gains, such as coherent or incoherent integration, were understood: that is, the expected value of the received signal is considered, provided the proper noise and speckle mitigation approaches are carried out.

B. Results and Discussion

For most SoOp scenarios, it is assumed that only coherent scattering takes place over land, so the incoherent component is neglected. This assumption relies only on the specular scattering driven by the Fresnel reflection coefficients. On the other hand, the reflected signals are generally a combination of both the coherent (specular) and incoherent (diffuse) scattering components. In **Fig. 9**, a comparison is presented between diffuse (the filled circle marker) and specular (the filled square marker) contributions over Paulownia trees as a function of observation angle (θ_s) at various receiver heights (20, 50, 100, 500 m). The left panel shows cross-polarized (RL – RHCP transmit, LHCP receive) received power while the right panel shows co-polarized (RR – RHCP

transmit, RHCP receive) received power. In the figure, the results of specular reflection from a bare soil is also added and is represented by filled diamond marker. As it can be seen, as the receiver altitude increases from 20 m to 500 m, the diffuse term in both polarization is greatly reduced due to multiplicative dependence of path loss of the diffuse term [see Eq. (21.d)] and the specular term remains the same since its path loss has a total path ray dependence [see Eq. (21.c)] and the receiver altitude is much smaller than orbits of the GEO satellites. Similar results were experimental observed by a GNSS-R balloon experiment where the received power did not change with the balloon height [13], indicating that the coherent term dominates the received signal.

It is evident from the results in Fig. 9 that the cross-polarized coherent term will always dominate the received power even for the receiver at low altitudes for flat terrains (i.e., in the absence of topographic relief) and cross-polarized diffuse term can thus be ignored. Similar result for cross-polarized reflected signals has been confirmed by spaceborne observations at L-band [3]. On the other hand, co-polarized diffuse term could be comparable or even larger than co-polarized specular term at lower incidence angles and low altitudes. As the incidence angle increases, co-polarized specular term starts to overpass the diffuse term again. This indicates that the reflected co-polarized signals could still include incoherent scattering components at low latitudes and the relative importance of these contributions is expected to vary with respect to the scene properties around the specular point and incidence angle. This has important implications for studies that use the co- and cross-polarization power ratio [9] to cancel out common factors and to make soil moisture inversion more robust against roughness. The diffuse contributions for low altitude observations should be included in the model and interpretation of the results since both specular and diffuse terms have different dependence on the path loss, polarization, and incidence angle.

716

717 The diffuse scattering includes volume scattering within canopy, double bounce effects due to soil
718 and trunk/canopy interactions, as well as attenuation by the vegetation canopy. **Fig. 10** provides
719 comparison between specular reflectivity of bare (square marker) and vegetation (diamond
720 marker), and effective NBRCSs (circular markers) of diffuse scattering mechanisms. It is well
721 known that ground reflection changes its polarization from right-hand to left-hand and vice versa.
722 The cross-polarization specular reflectivity is thus much higher than co-polarization reflectivity at
723 low incidence angles and both response merges as the angle approaches Brewster angle as shown
724 in the right panel of **Fig. 10**. The cross-polarization specular response of both bare and vegetation
725 shows a decreasing trend with increasing angle of observation, but the drop in vegetation
726 reflectivity is more substantial due to the increasing attenuation by the plant canopy with
727 increasing incidence angle.

728

729 In the left panel of **Fig. 10**, the effective NBRCS is decomposed into its scattering mechanisms;
730 single bounce, double bounce, and triple bounce. The single bounce shows no difference between
731 cross- and co- polarized signatures since it involves no ground reflection and the volume scattering
732 does not have any preference for circular polarization handedness. Similarly, the triple bounce
733 shows no polarization difference either since the wave bounces twice from the ground. The first
734 bounce changes RHCP to LHCP and the second bounce changes back to the RHCP. The triple
735 bounce is also the smallest contribution due to double ground reflection. On the other hand, as
736 seen in **Fig. 10**, the double bounce response produces the largest among the other mechanisms
737 since it bounces once from the ground and its scattering angle is well aligned with vertical trucks'
738 scattering cones, where the amplitude of the scattering has its maximum in a conical region [52].

739

740 There are some remarkable features in both polarimetric and angular response of NBRCS. First,
741 the cross-polarization NBRCS of the double bounce contribution is higher than co-polarization
742 NBRCS at low incidence angles and both response merges at higher angles. This is similar to the
743 specular reflectivity response, but the polarization difference is much smaller in NBRCS since
744 volume depolarization within vegetation combines two polarized components. This difference is
745 much smaller than the present antenna crosstalk, which is 25 dB. This indicates that depolarization
746 in vegetation is the main cause of this phenomena. Second, cross-polarization NBRCS response
747 shows an increasing trend up to $\sim 30^\circ$ incidence angle, and then decreases with increase in the
748 incidence angle in contrast to the cross-polarization specular reflectivity that always decreases with
749 the incidence angle.

750

751 Note that the both specular reflectivity and NBRCS of the vegetation depends not only on the
752 surface and vegetation parameters, but also on system parameters such as the receiving and
753 transmitting antenna parameters, and altitude. In **Fig. 11**, the effect of the receiver altitude on the
754 diffuse term is further investigated by including the antenna characteristics and Fresnel zones by
755 using expression in **Eq. (22.c)** that provides the explicit dependence of NBRCS on the system
756 parameters. In **Fig. 11(a)**, effective NBRCS is plotted against number of Fresnel zones at various
757 heights for ideal (nonfilled markers) and beam-limited (filled markers) antennas. The left panel
758 shows cross-polarized (RL) NBRCS while the right panel shows co-polarized (RR) NBRCS. As
759 can be seen from the figures, it is clear that (1) in both polarization, effective NBRCS decreases
760 as more Fresnel zones are included, (2) higher effective NBRCS is observed with higher altitudes,
761 and (3) at lower altitudes antenna radiation pattern plays a greater role in NBRCS values. It can

be clearly noticed that NBRCS, which should represent the scene scattering properties, are blended with the system parameters, particularly at lower altitudes. Most of the current studies are carried out from lower altitude platforms that are often used for validation of spaceborne instruments. In order to link these studies to spaceborne observation, the system related effects needs to be corrected to arrive at scene-only NBRCS.

Fig. 11 (b)-(d) shows the projection of the receiver antenna footprints and 10 Fresnel zones on the ground from 20 m, 50 m, 100 m and 500 m observing altitudes to provide further insight into the system related effects on NBRCS. As evident from these figures, the relative area covered by the same number of Fresnel zones with respect to antenna footprint gets reduced as the altitude increases. As a result, the scattering angles are confined around the boresight of the receiver antenna radiation pattern at higher altitudes as less decrease in NBRCS is observed at 500 m. When the results by using ideal (unit pattern matrix) and actual (beam-limited) antennas are compared, it is clear that even if we use pencil beam (ideal) antenna, the NBRCS still gets reduced as new Fresnel zones are included. This is due to the trunk's unique scattering patterns, which scatter most in a conical region. The scattering angles are much more spread at lower altitudes as seen in **Fig. 10 (b)-(d)**. The weaker scattered fields are observed in the bistatic direction associated with trunk-ground interaction since the scattered wave from vertical trunks becomes slightly away from the forward scattering cone. This scattering behavior of vertical trunks acts like a special filter and concentrates most of the power along the specular direction.

As stated earlier, the cross-polarization coherent scattering from vegetation over a flat ground almost always overpass the diffuse contribution to the received power. However co-polarization

diffuse power can be comparable or can even larger than co-polarization coherent received power. It is worth investigating the effect of diffuse contribution on the co-polarization specular reflectivity. **Fig. 12** shows effect of diffuse contribution in the first Fresnel zone as a function of altitude (the left panel) and at 20 m altitude as a function contributing Fresnel zones (the right panel). The filled square marker represents specular reflectivity [Eq. (22.b)] while smaller filled circles denote reflectivity of total received signal (specular + diffuse) [Eq. (29)]. As seen from the left panel, as the altitude increases (increasing altitude is indicated by an arrow in the figure), the total reflectivity approaches the specular reflectivity. The effect of diffuse scattering is more apparent at lower incidence angles. On the other hand, as more Fresnel zones are included (increasing Fresnel zones are indicated with an arrow in the figure), the total reflectivity diverges from the specular reflectivity, particularly at lower incidence angles. This increase in the total reflectivity is due to the including of additional diffuse scattering with more Fresnel zones. As a result, additional diffuse contributions to the total reflectivity will alter its angular signature as a function of both Fresnel zones and receiver height and can introduce errors on estimation of well-known Fresnel reflection coefficients that are often used in soil moisture retrievals. Diffuse scattering, although weak at high altitude, can have significant influence on co-polarization reflectivity observed by ground and airborne systems which are usually used as a testbed for algorithm development for spaceborne missions. If co-polarized signals are used in the retrievals, the co-polarized diffuse component should be included in the model for low altitude platforms.

IV. SUMMARY AND CONCLUSION

There is increasing interest to use reflected (or multipath) navigation and communication satellite signals for remote sensing of a number of geophysical land parameters such as soil moisture and biomass. Although the handful experimental and theoretical studies demonstrate the potential of spaceborne SoOp observations for such applications, there are many unknowns regarding the impacts of vegetation and system parameters on the observations. The scattering models are thus a critical means in advancement of these studies and in the design of future missions or field campaigns. In this paper, we presented an overview of the newly formulated coherent bistatic vegetation model, i.e. SCoBi-Veg, which simulates polarimetric reflectometry of vegetated landscapes using a Monte Carlo scheme. The model calculates the complex field in direct, specular, and diffuse terms by explicitly accounting for both system parameters (e.g., the antenna beamwidth, polarization crosstalk, polarization mismatch, altitude, etc.) and the statistical and physical properties of the terrain. In contrast to the previous studies that have usually assumed plane wave illumination/scattering, and/or ignored such antenna effects, the SCoBi-Veg model considers variations of both the strength and polarization states of the received wave along the beam direction so that the same model could be uniformly applied across different platforms at various altitudes.

P-band signals of geostationary communication satellites are considered as an application of the model. The coherent and diffuse components of the reflected signatures from tree canopies are compared for down-looking dual circular polarized receivers at various altitudes. It is shown that the cross-polarized coherent term dominates the received power over flat vegetated terrains, but

828 co-polarized diffuse term could be comparable or even larger than co-polarized specular term at
829 lower incidence angles and low altitudes. The diffuse scattering was decomposed into the
830 scattering mechanisms and the double bounce was shown to be the main contributor. Furthermore,
831 the double bounce from the vertical trunks acts like a special filter and concentrates most of the
832 reflected power along the specular direction. The effect of antenna beamwidth and altitude on the
833 diffuse scattering was also quantified. It is shown that the NBRCS, which should represent the
834 scene scattering properties, are blended with the system parameters, particularly at lower altitudes.
835 Even though the relative contribution of the NBRCS to the total reflectivity is inversely
836 proportional to the receiver height, diffuse scattering can still alter angular signature of co-
837 polarized reflectivity as a function of both Fresnel zones and receiver height. This can introduce
838 errors on estimation of well-known Fresnel reflection coefficients that are often used in soil
839 moisture retrievals. If co-polarized signals are used in the retrievals, the co-polarized diffuse
840 component should be included in the model for low altitude platforms and be corrected for antenna
841 and altitude effects.

APPENDIX A: *Normalized “Voltage” Pattern*

In this appendix, the normalized “voltage pattern” for both linear and circular polarization basis will be expressed. Due to reciprocity, the following arguments are equally applicable for antennas in transmit and receive modes.

In practice, antennas cannot be constructed to produce pure polarization states [37]. It is important to decompose the radiated field into two orthonormal polarization states. The orthogonal polarization states are commonly chosen along the linear or circular basis vectors. For linear basis, co-polarized and cross-polarized patterns are defined for each port as

$$\mathbf{g}_X = g_{XX}\hat{\mathbf{u}}_1^X + g_{XY}\hat{\mathbf{u}}_2^Y \quad (\text{A.1a})$$

$$\mathbf{g}_Y = g_{YX}\hat{\mathbf{u}}_1^X + g_{YY}\hat{\mathbf{u}}_2^Y \quad (\text{A.1b})$$

where g_{XX} is the co-polarized voltage pattern for port 1 while g_{XY} is the cross-polarized voltage pattern for the same port. The quantity g_{YY} is the co-polarized voltage pattern for port 2 while g_{YX} is the cross-polarized voltage pattern for the same port. The voltage patterns are complex. The cross-polarized patterns represent the crosstalk between antenna ports. The unit vectors $\hat{\mathbf{u}}_1^X$ and $\hat{\mathbf{u}}_2^Y$ are also complex and are associated with co-polarization and cross-polarization states.

In linear basis, the polarization vectors are chosen according to Ludwig’s third definition of polarization to indicate the directions of co-polarization and cross-polarization [53]. They are rotated versions of spherical vectors defined in antenna coordinates and can be written as

863

$$\hat{\mathbf{u}}_1^X = \cos \varphi \hat{\boldsymbol{\theta}} - \sin \varphi \hat{\boldsymbol{\phi}} \quad (\text{A.2a})$$

$$\hat{\mathbf{u}}_2^Y = \sin \varphi \hat{\boldsymbol{\theta}} + \cos \varphi \hat{\boldsymbol{\phi}} \quad (\text{A.2b})$$

864

865 where $\hat{\boldsymbol{\theta}}$ and $\hat{\boldsymbol{\phi}}$ are the unit vectors in spherical coordinates of the antenna. Thus, the normalized

866 “voltage” pattern matrix for the linearly polarized antenna is given as

867

$$\underline{\underline{g}} = \begin{bmatrix} g_{XX} & g_{XY} \\ g_{YX} & g_{YY} \end{bmatrix} \quad (\text{A.3})$$

868

869 For right-hand circular polarization (RHCP) as the reference polarization and left-hand circular

870 polarization (LHCP) as the cross-polarization, the unit polarization vectors are

871

$$\hat{\mathbf{u}}_1^R = \frac{1}{\sqrt{2}} (\hat{\mathbf{u}}_1^X - i \hat{\mathbf{u}}_2^Y) \quad (\text{A.4a})$$

$$\hat{\mathbf{u}}_2^L = \frac{1}{\sqrt{2}} (\hat{\mathbf{u}}_1^X + i \hat{\mathbf{u}}_2^Y) \quad (\text{A.4b})$$

872

873 Similarly, for circular polarization basis, co-polarized and cross-polarized patterns can be written

874 for each port as

$$\mathbf{g}_R = g_{RR} \hat{\mathbf{u}}_1^R + g_{RL} \hat{\mathbf{u}}_2^L \quad (\text{A.5a})$$

$$\mathbf{g}_L = g_{LR} \hat{\mathbf{u}}_1^R + g_{LL} \hat{\mathbf{u}}_2^L \quad (\text{A.5b})$$

875

876 where the subscripts/superscripts R and L denotes RHCP and LHCP, respectively. The normalized

877 “voltage” pattern matrix for the circularly polarized antenna is given as

878

$$\underline{\underline{g}} = \begin{bmatrix} g_{RR} & g_{RL} \\ g_{LR} & g_{LL} \end{bmatrix} \quad (\text{A.6})$$

879

880 where the diagonal elements are co-polarized patterns while the off-diagonal elements are cross-
881 polarized patterns. The elements are all complex.

882

APPENDIX B: Polarization Basis Transformation

An arbitrary polarized electric field can always be expressed by linear combination of two orthogonal (basis) fields that are usually defined in one coordinate system [54]. Since bistatic scattering involves radiation, scattering, and reception in various coordinate systems, it is necessary to transform polarization basis vectors in one coordinate system to another one. In this appendix, we will consider two configurations: Transmit-Receive, Transmit-Scattering-Receive as depicted in **Fig. 6**.

B.1 Transmit-Receive Configuration

Let us first consider two arbitrary oriented antenna coordinate systems that are represented by $T: (x_t, y_t, z_t)$ and $R: (x_r, y_r, z_r)$ as shown in **Fig. 6(a)**. The unit vectors $\hat{\mathbf{u}}_{t1}$ and $\hat{\mathbf{u}}_{t2}$ are complex orthonormal and defined in the transmit antenna system T while the unit vectors $\hat{\mathbf{u}}_{r1}$ and $\hat{\mathbf{u}}_{r2}$ are complex orthonormal and defined in the receive antenna system R . An arbitrary electrical field can be decomposed into orthogonal components in both systems as

$$\mathbf{E} = E_{t1}\hat{\mathbf{u}}_{t1} + E_{t2}\hat{\mathbf{u}}_{t2} \quad (\text{B.1a})$$

$$\mathbf{E} = E_{r1}\hat{\mathbf{u}}_{r1} + E_{r2}\hat{\mathbf{u}}_{r2} \quad (\text{B.1b})$$

The components of the field in both coordinates are related as

$$E_{r1} = \mathbf{E} \cdot \hat{\mathbf{u}}_{r1}^* = E_{t1}(\hat{\mathbf{u}}_{t1} \cdot \hat{\mathbf{u}}_{r1}^*) + E_{t2}(\hat{\mathbf{u}}_{t2} \cdot \hat{\mathbf{u}}_{r1}^*) \quad (\text{B.2a})$$

$$E_{r2} = \mathbf{E} \cdot \hat{\mathbf{u}}_{r2}^* = E_{t1}(\hat{\mathbf{u}}_{t1} \cdot \hat{\mathbf{u}}_{r2}^*) + E_{t2}(\hat{\mathbf{u}}_{t2} \cdot \hat{\mathbf{u}}_{r2}^*) \quad (\text{B.2b})$$

902 The above equations can be cast into a matrix form as

903

$$\begin{bmatrix} E_{r1} \\ E_{r2} \end{bmatrix} = \underline{\underline{u}}_{t \rightarrow r} \begin{bmatrix} E_{t1} \\ E_{t2} \end{bmatrix} \quad (\text{B.3a})$$

904

905 where the transformation matrix $\underline{\underline{u}}_{t \rightarrow r}$ is given by

906

$$\underline{\underline{u}}_{t \rightarrow r} = \begin{bmatrix} \hat{\mathbf{u}}_{t1} \cdot \hat{\mathbf{u}}_{r1}^* & \hat{\mathbf{u}}_{t2} \cdot \hat{\mathbf{u}}_{r1}^* \\ \hat{\mathbf{u}}_{t1} \cdot \hat{\mathbf{u}}_{r2}^* & \hat{\mathbf{u}}_{t2} \cdot \hat{\mathbf{u}}_{r2}^* \end{bmatrix} \quad (\text{B.3b})$$

907

908 where it transforms polarization components of the system T to those in the system R . The matrix
 909 is, in fact, a unitary matrix that conserves the total power of a wave, that is, the norm of the electric
 910 field vector remains invariant under change of basis [54]. As a result, the inverse of the
 911 transformation matrix (or transformation from R to T) is

912

$$\underline{\underline{u}}_{r \rightarrow t} = \underline{\underline{u}}_{t \rightarrow r}^{-1} = \underline{\underline{u}}_{t \rightarrow r}^H \quad (\text{B.4})$$

913

914 where superscript -1 and H are the inverse and the Hermitian (or conjugate) transpose of a matrix,
 915 respectively.

916

917 Now let us consider the unit spherical vectors (orthogonal sets) in both coordinate systems. The
 918 direction of propagation is represented by $\hat{\mathbf{k}}_d$ vector that connects origins of both coordinate
 919 systems. It is evident that the transmit antenna spherical vectors $(\hat{\boldsymbol{\theta}}_t, \hat{\boldsymbol{\phi}}_t)$ lie in the same tangential

plane (tangent plane 1), where the receive antenna spherical vectors $(\hat{\boldsymbol{\theta}}_r, \hat{\boldsymbol{\varphi}}_r)$ lie, and both of which are normal to $\hat{\mathbf{k}}_d$, as illustrated in **Fig. 6(a)**, due to the following orthogonality relationship:

$$\hat{\boldsymbol{\varphi}}_t \times \hat{\mathbf{k}}_d = \hat{\boldsymbol{\theta}}_t \quad \text{and} \quad \hat{\mathbf{k}}_d \times \hat{\boldsymbol{\theta}}_t = \hat{\boldsymbol{\varphi}}_t \quad (\text{B.5a})$$

$$\hat{\mathbf{k}}_d \times \hat{\boldsymbol{\varphi}}_r = \hat{\boldsymbol{\theta}}_r \quad \text{and} \quad \hat{\boldsymbol{\theta}}_r \times \hat{\mathbf{k}}_d = \hat{\boldsymbol{\varphi}}_r \quad (\text{B.5b})$$

The linear and circular basis vectors (defined in **Eqs. A.2 and A.4**) also lie on the same tangent plane since they are rotated versions of spherical vectors defined in their respective coordinate systems. As a result, the transformation matrix, $\underline{\underline{u}}_{t \rightarrow r}$, is, in fact, a rotation matrix between any polarization basis (within the system T or R and between the systems T and R), defined in the same tangential plane. In other words, any polarization states defined along a direct path between the origins of two arbitrary coordinate systems are related via a rotation matrix. One can go from one polarization basis to another one by simply substituting the unit complex polarization vector pairs [i.e., $(\hat{\boldsymbol{\theta}}_t, \hat{\boldsymbol{\varphi}}_t)$, $(\hat{\mathbf{u}}_{t1}^R, \hat{\mathbf{u}}_{t2}^L)$, $(\hat{\mathbf{u}}_{t1}^X, \hat{\mathbf{u}}_{t2}^Y)$, $(\hat{\boldsymbol{\theta}}_r, \hat{\boldsymbol{\varphi}}_r)$, $(\hat{\mathbf{u}}_{r1}^R, \hat{\mathbf{u}}_{r2}^L)$, and $(\hat{\mathbf{u}}_{r1}^X, \hat{\mathbf{u}}_{r2}^Y)$] in the rotation matrix given in **Eq. (B.3b)**.

B.2 Transmit-Scattering-Receive Configuration

Now we add an intermediate coordinate system (x', y', z') to represent local scattering processes between transmit and receive antennas as shown in **Fig. 6(b)**. In this configuration, the transformation involves two rotation matrices; one is from the transmit antenna to the ground system and the other one is from the ground system to the receive antenna. The incoming and outgoing propagation vectors, $\hat{\mathbf{k}}_i$ and $\hat{\mathbf{k}}_o$ can be defined and be written in local coordinates by

$$-\hat{\mathbf{k}}_i = \hat{\mathbf{x}}' \sin \theta'_i \cos \varphi'_i + \hat{\mathbf{y}}' \sin \theta'_i \sin \varphi'_i + \hat{\mathbf{z}}' \cos \theta'_i \quad (\text{B.7a})$$

$$\hat{\mathbf{k}}_o = \hat{\mathbf{x}}' \sin \theta'_o \cos \varphi'_o + \hat{\mathbf{y}}' \sin \theta'_o \sin \varphi'_o + \hat{\mathbf{z}}' \cos \theta'_o \quad (\text{B.7b})$$

where the angles (θ'_i, φ'_i) and (θ'_o, φ'_o) represent the angle of incidence and the angle of scattering in the local coordinate system, respectively. The propagation vector, $\hat{\mathbf{k}}_i$, is normal to both the transmit antenna spherical vectors $(\hat{\boldsymbol{\theta}}_t, \hat{\boldsymbol{\phi}}_t)$ and the local spherical vectors $(\hat{\boldsymbol{\theta}}'_i, \hat{\boldsymbol{\phi}}'_i)$ along the angle (θ'_i, φ'_i) while the propagation vector, $\hat{\mathbf{k}}_o$, is normal to both the receive antenna spherical vectors $(\hat{\boldsymbol{\theta}}_r, \hat{\boldsymbol{\phi}}_r)$ and the local spherical vectors $(\hat{\boldsymbol{\theta}}'_o, \hat{\boldsymbol{\phi}}'_o)$ along the angle (θ'_o, φ'_o) . Due to these orthogonality relationships, we can define a tangent plane (tangent plane 2) between the transmit antenna and the ground, and can define another tangent plane (tangent plane 3) between the receive antenna and the ground. The unit vectors $(\hat{\mathbf{u}}_{t1}, \hat{\mathbf{u}}_{t2})$ and $(\hat{\mathbf{u}}_{r1}, \hat{\mathbf{u}}_{r2})$ also lie in the tangent planes 2 and 3, respectively. Thus, the rotation matrices from the transmit antenna to the ground and the ground to the receive antenna can be written as

$$\underline{\underline{u}}_{t \rightarrow g}(\hat{\mathbf{k}}_i) = \begin{bmatrix} \hat{\mathbf{u}}_{t1} \cdot \hat{\mathbf{v}}_i^* & \hat{\mathbf{u}}_{t2} \cdot \hat{\mathbf{v}}_i^* \\ \hat{\mathbf{u}}_{t1} \cdot \hat{\mathbf{h}}_i^* & \hat{\mathbf{u}}_{t2} \cdot \hat{\mathbf{h}}_i^* \end{bmatrix} \quad (\text{B.8a})$$

and

$$\underline{\underline{u}}_{g \rightarrow r}(\hat{\mathbf{k}}_o) = \begin{bmatrix} \hat{\mathbf{v}}_o \cdot \hat{\mathbf{u}}_{r1}^* & \hat{\mathbf{h}}_o \cdot \hat{\mathbf{u}}_{r1}^* \\ \hat{\mathbf{v}}_o \cdot \hat{\mathbf{u}}_{r2}^* & \hat{\mathbf{h}}_o \cdot \hat{\mathbf{u}}_{r2}^* \end{bmatrix} \quad (\text{B.8b})$$

where $(\hat{\mathbf{u}}_{t1}, \hat{\mathbf{u}}_{t2})$ and $(\hat{\mathbf{u}}_{r1}, \hat{\mathbf{u}}_{r2})$ can be the linearly polarized or circularly polarized unit vectors as defined in **Eqs. (A.2) and (A.4)**. The local horizontal polarization vector, $\hat{\mathbf{h}}_o$, for scattered wave is taken parallel to the local ground $(x' - y')$ plane. More specifically,

$$\hat{\mathbf{h}}_o = \frac{\hat{\mathbf{n}} \times \hat{\mathbf{k}}_o}{|\hat{\mathbf{n}} \times \hat{\mathbf{k}}_o|} = \hat{\boldsymbol{\varphi}}'_o \quad (\text{B.9a})$$

959

960 The local vertical polarization is taken perpendicular to both $\hat{\mathbf{k}}_o$ and $\hat{\mathbf{h}}_o$; thus

961

$$\hat{\mathbf{v}}_o = \hat{\mathbf{h}}_o \times \hat{\mathbf{k}}_o = \hat{\boldsymbol{\theta}}'_o \quad (\text{B.9b})$$

962

963 Similarly, the local horizontal polarization vector, $\hat{\mathbf{h}}_i$, for incident wave is taken parallel to the

964 local ground ($x' - y'$) plane. More specifically,

965

$$\hat{\mathbf{h}}_i = \frac{\hat{\mathbf{k}}_i \times \hat{\mathbf{n}}}{|\hat{\mathbf{k}}_i \times \hat{\mathbf{n}}|} = \hat{\boldsymbol{\varphi}}'_i \quad (\text{B.10a})$$

966

967 The local vertical polarization is taken perpendicular to both $\hat{\mathbf{k}}_i$ and $\hat{\mathbf{h}}_i$; thus

968

$$\hat{\mathbf{v}}_i = \hat{\mathbf{k}}_i \times \hat{\mathbf{h}}_i = \hat{\boldsymbol{\theta}}'_i \quad (\text{B.10b})$$

969

APPENDIX C: Antenna Rotation Matrices

The received field expressions derived in the main text assume knowledge of the relationship between various coordinate systems. In this appendix, we define coordinate transformation between the antenna coordinates and the reference coordinate system. Let us consider the receive antenna here but the same is also applicable to the transmit antenna. The antenna coordinate system is rotated about the z -axis by φ_{0r} in azimuth. Then, the antenna is rotated about the y -axis by $(\pi - \theta_{0r})$ in elevation. These rotations are illustrated in **Fig. 7**. The angle φ_{0r} is defined counter clockwise from the x -axis while the angle θ_{0r} is defined counterclockwise from the $-z$ -axis. When $\varphi_{0r} = 0$, the antenna is facing East and when $\varphi_{0r} = \pi/2$, the antenna is facing North. The azimuth rotation is performed for aligning the direction of the incident field from a satellite. When $\theta_{0r} = 0$, the antenna is facing nadir and when $\theta_{0r} = \pi$, the antenna is facing zenith. The angle θ_{0r} represents the observation angle. With these rotations, the antenna y_r -axis will always be parallel to the ground ($x - y$ plane), so that it can represent the horizontal polarized port when the antenna is linearly polarized. The rotation matrices from the antenna to the reference system in elevation and azimuth planes are, respectively, given by:

$$[A]_{\theta_{0r}} = \begin{bmatrix} -\cos \theta_{0r} & 0 & \sin \theta_{0r} \\ 0 & 1 & 0 \\ -\sin \theta_{0r} & 0 & -\cos \theta_{0r} \end{bmatrix} \quad (\text{C.1})$$

$$[A]_{\varphi_{0r}} = \begin{bmatrix} \cos \varphi_{0r} & -\sin \varphi_{0r} & 0 \\ \sin \varphi_{0r} & \cos \varphi_{0r} & 0 \\ 0 & 0 & 1 \end{bmatrix} \quad (\text{C.2})$$

Because the rotation matrix is orthogonal, transformation in the reverse direction is simply the transpose of the matrix.

APPENDIX D: Outer Product Matrices and Vectors

The outer product is defined for two element vectors by [55]:

$$\underline{P} = \underline{b} \otimes \underline{b}^* = \begin{bmatrix} b_1 \underline{b}^* \\ b_2 \underline{b}^* \end{bmatrix} = \begin{bmatrix} b_1 b_1^* \\ b_1 b_2^* \\ b_2 b_1^* \\ b_2 b_2^* \end{bmatrix} \quad (\text{D.1})$$

and for the two by two matrix of a circularly polarized antenna by

$$\begin{aligned} \underline{\underline{G}} = \underline{\underline{g}} \otimes \underline{\underline{g}}^* &= \begin{bmatrix} g_{RR} \underline{\underline{g}}^* & g_{RL} \underline{\underline{g}}^* \\ g_{LR} \underline{\underline{g}}^* & g_{LL} \underline{\underline{g}}^* \end{bmatrix} \\ &= \begin{bmatrix} g_{RR} g_{RR}^* & g_{RR} g_{RL}^* & g_{RL} g_{RR}^* & g_{RL} g_{RL}^* \\ g_{RR} g_{LR}^* & g_{RR} g_{LL}^* & g_{RL} g_{LR}^* & g_{RL} g_{LL}^* \\ g_{LR} g_{RR}^* & g_{LR} g_{RL}^* & g_{LL} g_{RR}^* & g_{LL} g_{RL}^* \\ g_{LR} g_{LR}^* & g_{LR} g_{LL}^* & g_{LL} g_{LR}^* & g_{LL} g_{LL}^* \end{bmatrix} \end{aligned} \quad (\text{D.2})$$

The elements of the coherency vector and matrix are complex, and it is sometimes desirable to describe the wave by real quantities. The modified Stokes vector is commonly used in microwave remote sensing to describe both amplitude and polarization of the wave [43]. It is a transform of the coherency vector. The modified Stokes vector of the total power is given by:

$$\underline{P}_M = \underline{\underline{Q}} \cdot \underline{P} = \begin{bmatrix} |b_1|^2 \\ |b_2|^2 \\ 2\text{Re}\{b_1 b_2^*\} \\ 2\text{Im}\{b_1 b_2^*\} \end{bmatrix} \quad (\text{D.3})$$

1003 where

$$\underline{\underline{Q}} = \begin{bmatrix} 1 & 0 & 0 & 0 \\ 0 & 0 & 0 & 1 \\ 0 & 1 & 1 & 0 \\ 0 & -i & -i & 0 \end{bmatrix} \quad (\text{D.4})$$

1004

1005 Similarly, the four-by-four Mueller matrix of a circularly polarized antenna can be defined for the

1006 modified Stokes vector as

1007

$$\underline{\underline{G}}_M = \underline{\underline{Q}} \cdot \underline{\underline{G}} \cdot \underline{\underline{Q}}^{-1}$$

$$= \begin{bmatrix} |g_{RR}|^2 & |g_{RL}|^2 & \text{Re}\{g_{RR}g_{RL}^*\} & -\text{Im}\{g_{RR}g_{RL}^*\} \\ |g_{LR}|^2 & |g_{LL}|^2 & \text{Re}\{g_{LL}g_{LR}^*\} & \text{Im}\{g_{LL}g_{LR}^*\} \\ 2\text{Re}\{g_{RR}g_{LR}^*\} & 2\text{Re}\{g_{LL}g_{RL}^*\} & \text{Re}\{g_{RR}g_{LL}^* + g_{RL}g_{LR}^*\} & -\text{Im}\{g_{RR}g_{LL}^* + g_{RL}g_{LR}^*\} \\ 2\text{Im}\{g_{RR}g_{LR}^*\} & -2\text{Im}\{g_{LL}g_{RL}^*\} & \text{Im}\{g_{RR}g_{LL}^* + g_{RL}g_{LR}^*\} & \text{Re}\{g_{RR}g_{LL}^* - g_{RL}g_{LR}^*\} \end{bmatrix}$$

1010 (D.5)

1011

1012

- [1] J. Garrison, E. Cardellach, S. Gleason and S. J. Katzberg, "Foreword to special issue on reflectometry using global navigation satellite systems and other signals of opportunity (GNSS+R)," *IEEE J. Sel. Topics Appl. Earth Observ. Remote Sens.*, vol. 7, no. 5, p. 1412–1415, 2014.
- [2] E. Cardellach, S. Vey and J. Wickert, "Foreword to the Special Issue on GNSS Reflectometry," *IEEE J. Sel. Topics Appl. Earth Observ. Remote Sens.*, vol. 9, no. 10, p. 4519–4524, 2016.
- [3] M. Unwin, P. Jales, J. Tye, C. Gommenginger, G. Foti and J. Rosello, "Spaceborne GNSS-reflectometry on TechDemoSat-1: Early mission operations and exploitation," *IEEE J. Sel. Top. Appl. Earth Observ. Remote Sens.*, vol. 9, no. 10, p. 4525–4539, 2016.
- [4] S. Gleason, S. Hodgart, Y. Sun, C. Gommenginger, S. Mackin, M. Adjrard and M. Unwin, "Detection and processing bistatically reflected GPS signals from low earth orbit for the purposes of ocean remote sensing," *IEEE Trans. Geosci. Remote Sens.*, vol. 43, no. 6, p. 1229–1241, 2005.
- [5] C. Ruf, M. Unwin, J. Dickinson, R. Rose, D. Rose, M. Vincent and A. Lyons, "CYGNSS: Enabling the future of hurricane prediction," *IEEE Geosci. Remote Sens. Mag.*, vol. 1, no. 2, p. 52–67, 2013.
- [6] U. V. Zavorotny, S. Gleason, E. Cardellach and A. Camps, "Tutorial on remote sensing using GNSS bistatic radar of opportunity," *IEEE Geosci. Remote Sens. Mag.*, vol. 2, no. 4, p. 8–45, 2014.
- [7] N. Rodriguez-Alvarez, A. Camps, M. Vall-Llossera, X. Bosch-Lluis, A. Monerris, I. Ramos-Perez, E. Valencia, J. Marchan-Hernandez, J. Martinez-Fernandez and G. Baroncini-Turricchia, "Land Geophysical Parameters Retrieval Using the Interference Pattern GNSS-R Technique," *IEEE Trans. Geosci. Remote Sens.*, vol. 49, no. 1, p. 71–84, 2011.
- [8] A. Alonso-Arroyo, A. Camps, A. Aguasca, G. Forte, A. Monerris, C. Rudiger, J. Walker, H. Park, D. Pascual and R. Onrubia, "Dual-polarization GNSS-R interference pattern technique for soil moisture mapping," *IEEE J. Sel. Topics Appl. Earth Obs. Remote Sens.*, vol. 7, no. 5, p. 1533–1544, 2014.
- [9] A. Egido, M. Caparrini, G. Ruffini, S. Paloscia, E. Santi, L. Guerriero, N. Pierdicca and N. Floury, "Global Navigation Satellite Systems reflectometry as a remote sensing tool for agriculture," *Remote Sens.*, vol. 4, no. 8, p. 2356–2372, 2012.
- [10] K. M. Larson, J. J. Braun, E. E. Small, V. U. Zavorotny, E. D. Gutmann and A. L. Bilich, "GPS Multipath and its relation to near-surface soil moisture content," *IEEE J. Sel. Topics Appl. Earth Observ. Remote Sens.*, vol. 3, no. 1, pp. 91–99, 2010.
- [11] C. C. Chew, E. Small, K. M. Larson and V. U. Zavorotny, "Vegetation sensing using GPS-interferometric reflectometry: theoretical effects of canopy parameters on signal-to-noise ratio data," *IEEE Trans Geosci Remote Sens.*, vol. 53, no. 5, p. 2755–2764, 2015.
- [12] A. Egido, S. Paloscia, E. Motte, L. Guerriero, N. Pierdicca, M. Caparrini, E. Santi, G. Fontanelli and F. N., "Airborne GNSS-R polarimetric measurements for soil moisture and above-ground

- biomass estimation," *IEEE J. Sel. Topics Appl. Earth Obs. Remote Sens.*, vol. 7, no. 5, p. 1522–1532, 2014.
- [13] H. Carreno-Luengo, A. Camps, J. Querol and G. Forte, "First results of a GNSS-R experiment from a stratospheric balloon over boreal forests," *IEEE Trans. Geosci. Remote Sens.*, vol. 54, no. 5, pp. 2652 - 2663, 2016.
- [14] C. Chew, R. Shah, C. Zuffada, G. Hajj, D. Masters and A. J. Mannucci, "Demonstrating soil moisture remote sensing with observations from the UK TechDemoSat-1 satellite mission," *Geophys. Res. Lett.*, vol. 43, no. 7, p. 3317–3324, 2016.
- [15] A. Camps, H. Park, M. Pablos, G. Foti, C. P. Gommenginger, P. W. Liu and J. Judge, "Sensitivity of GNSS-R spaceborne observations to soil moisture and vegetation," *IEEE J. Sel. Topics Appl. Earth Observ. Remote Sens.*, vol. 9, no. 10, p. 4730–4742, 2016.
- [16] S. V. Nghiem, C. Zuffada, R. Shah, C. Chew, S. T. Lowe, A. J. Mannucci, E. Cardellach, G. R. Brakenridge, G. Geller and A. Rosenqvist, "Wetland monitoring with Global Navigation Satellite System reflectometry," *Earth and Space Science*, vol. 4, no. 1, p. 16–39, 2017.
- [17] R. Shah, C. Zuffada, C. Chew, M. Lavalley, X. Xu and A. Azemati, "Modeling Bistatic Scattering Signatures from Sources of Opportunity in P- Ka bands," in *International Conference on Electromagnetics in Advanced Applications (ICEAA)*, Verona, Italy, 2017.
- [18] R. Shah, J. L. Garrison and M. S. Grant, "Demonstration of Bistatic Radar for Ocean Remote Sensing Using Communication Satellite Signals," *IEEE Geoscience and Remote Sensing Letters*, vol. 9, no. 4, p. 619–623, 2012.
- [19] R. Shah, J. L. Garrison, A. Egido and G. Ruffini, "Bistatic radar measurements of significant wave height using signals of opportunity in l-, s-, and ku-bands," *IEEE Trans. Geosci. Remote Sens.*, vol. 54, no. 2, p. 826–841, 2016.
- [20] A. T. Joseph, M. Deshpande, P. E. O'Neill and L. Miles, "Development of VHF (240–270 MHz) Antennas for SoOp (Signal of Opportunity) Receiver for 6U Cubesat Platforms," in *Progress In Electromagnetic Research Symposium (PIERS)*, Shanghai, China, 2016.
- [21] J. Garrison, B. Nold, Y.-C. Lin, G. Pignotti, J. R. Piepmeier, M. Veg, M. Fritts, C. DuToit and J. Knuble, "Recent results on soil moisture remote sensing using P-band signals of opportunity," in *International Conference on Electromagnetics in Advanced Applications (ICEAA)*, Verona, Italy, 2017.
- [22] S. Yueh, R. Shah, X. Xu, K. Elder, C. S. Chae, S. Margulis, G. Liston, M. Durand and C. Derksen, "HydroCube mission concept: P-Band signals of opportunity for remote sensing of snow and root zone soil moisture," in *SPIE 10423, Sensors, Systems, and Next-Generation Satellites XXI*, Warsaw, Poland, 2017.
- [23] R. Shah, X. Xu, S. Yueh, C. S. Chae, K. Elder, B. Starr and Y. Kim, "Remote Sensing of Snow Water Equivalent Using P-Band Coherent Reflection," *IEEE Geoscience and Remote Sensing Letters*, vol. 14, no. 3, p. 309–313, 2017.

- [24] M. Kurum, M. Deshpande, A. T. Joseph, P. O'Neill, R. Lang and O. Eroglu, "Development of a Coherent Bistatic Vegetation Model for Signal of Opportunity Applications at VHF/UHF-bands," in *IEEE Int. Geoscience Remote Sensing Symp.*, Fort Worth, Texas, 2017.
- [25] P. Liang, L. Pierce and M. Moghaddam, "Radiative transfer model for microwave bistatic scattering from forest canopies," *IEEE Trans. Geosci. Remote Sens.*, vol. 43, no. 11, pp. 2470-2483, 2005.
- [26] P. Ferrazzoli, L. Guerriero, N. Pierdicca and R. Rahmoune, "Forest biomass monitoring with GNSS-R: Theoretical simulations," *Advances in Space Research*, vol. 47, no. 10, pp. 1823-1832, 2010.
- [27] L. Guerriero, N. Pierdicca, L. Pulvirenti and P. Ferrazzoli, "Use of satellite radar bistatic measurements for crop monitoring: A simulation study on corn field," *Remote Sens.*, vol. 5, no. 2, pp. 864-890, 2013.
- [28] N. Pierdicca, L. Guerriero, R. Giusto, M. Brogioni and A. Egido, "SAVERS: A simulator of GNSS reflections from bare and vegetated soils," *IEEE Trans. Geosci. Remote Sens.*, vol. 52, no. 10, p. 6542–6554, 2014.
- [29] X. R. Wu and S. G. Jin, "GNSS-Reflectometry: Forest canopies polarization scattering properties and modeling," *Advances in Space Research*, vol. 54, no. 5, pp. 863-870, 2014.
- [30] L. Thirion-Lefevre, E. Colin-Koeniguer and C. Dahon, "Bistatic scattering from forest components. Part I: coherent polarimetric modelling and analysis of simulated results," *Waves in Random and Complex Media*, vol. 20, no. 1, p. 36–61, 2010.
- [31] D. E. Kerr, "Propagation of Short Radio Waves," in *M.I.T. Radiation Laboratory Series, Vol. 13*, New York-London, McGraw-Hill, 1951, p. Section 5.4.
- [32] D. M. LeVine, R. Meneghini, R. H. Lang and S. S. Seker, "Scattering from arbitrarily oriented dielectric disks in the physical optics regime," *J. Opt. Soc. Amer.*, vol. 73, no. 10, p. 1255–1262, 1983.
- [33] D. M. LeVine, A. Schneider, R. H. Lang and H. G. Carter, "Scattering from thin dielectric disks," *IEEE Trans. Antennas Propag.*, vol. 33, no. 12, p. 1410–1413, 1985.
- [34] S. S. Seker and A. Schneider, "Electromagnetic scattering from a dielectric cylinder of finite length," *IEEE Trans. Antennas Propag.*, vol. 36, no. 2, p. 303–307, 1988.
- [35] M. Karam, A. Fung and Y. Antar, "Electromagnetic wave scattering from some vegetation samples," *IEEE Trans. Geosci. Remote Sens.*, vol. 26, no. 6, p. 799–808, 1988.
- [36] W. Wasylkiwskyj, "Response of an antenna to arbitrary incident fields," in *Antennas and Propagation Society International Symposium*, Washington, DC, 2005.
- [37] H. Mott, *Polarization in Antennas and Radar*, New York: John Wiley and Sons, In, 1986.

- [38] R. H. Lang, R. Landry, O. Kavaklioglu and J. C. Deguise, "Simulation of microwave backscatter from a red pine stand," in *SPIE, Multispectral Microw. Sens. Forestry, Hydrol. Natural Resources*, Rome, Italy, 1994.
- [39] R. H. Lang, "Electromagnetic backscattering from a random distribution of lossy dielectric scatterers," *Radio Sci.*, vol. 16, no. 1, p. 15–30, 1981.
- [40] L. L. Foldy, "The multiple scattering of waves. I. General theory of isotropic scattering by randomly distributed scatterers," *Phys. Rev.*, vol. 67, p. 107–119, 1945.
- [41] M. Lax, "Multiple scattering of waves," *Rev. Mod. Phys.*, vol. 23, p. 287–310, 1951.
- [42] B. J. Choudhury, T. J. Schmugge, R. W. Newton and A. Chang, "Effect of surface roughness on the microwave emission from soils," *J. Geophys. Res.*, vol. 84, no. C6, p. 5699–5706, 1979.
- [43] L. Tsang, J. A. Kong and R. T. Shin, *Theory of Microwave Remote Sensing*, New York: Wiley, 1985.
- [44] M. Kurum, "L-band Estimation of Forest Canopy Attenuation by a Time-Domain Analysis of Radar Backscatter Response," Ph.D. dissertation, The George Washington University, Washington, DC, 2009.
- [45] A. Ishimaru, *Wave Propagation and Scattering in Random Media*, vol. 1. ch. 5.4, New York.: Academic Press, 1978.
- [46] S. J. Katzberg and J. L. Garrison, "Utilizing GPS to Determine Ionospheric Delay over the Ocean," NASA Tech. Memo 4750, Washington, DC, 1996.
- [47] G. A. Hajj and C. Zuffada, "Theoretical description of a bistatic system for ocean altimetry using the GPS signal," *Radio Sci.*, vol. 38, no. 5, p. 1–10, 2003.
- [48] M. Kurum, R. H. Lang, P. E. O'Neill, A. T. Joseph, T. J. Jackson and M. H. Cosh, "A first-order radiative transfer model for microwave radiometry of forest at L-band," *IEEE Trans. Geosci. Remote Sens.*, vol. 49, no. 9, p. 3167–3179, 2011.
- [49] T. Castel, A. Beaudoin, N. Flourey, T. Le Toan, Y. Caraglio and J.-F. Barczi, "Deriving forest canopy parameters for backscatter models using the AMAP architectural plant model," *IEEE Trans. Geosci. Remote Sens.*, vol. 39, no. 3, p. 571–583, 2001.
- [50] Y.-C. Lin and K. Sarabandi, "A monte carlo coherent scattering model for forest canopies using fractal-generated trees," *IEEE Trans. Geosci. Remote Sens.*, vol. 37, no. 1, p. 440–451, 1999.
- [51] S. J. Katzberg, O. Torres, M. S. Grant and D. Masters, "Utilizing calibrated GPS reflected signals to estimate soil reflectivity and dielectric constant: Results from SMEX02," *Remote Sens. Environ.*, vol. 100, no. 1, p. 17–28, 2006.
- [52] P. deMatthaeis and R. H. Lang, "Microwave scattering models for cylindrical vegetation components," *Progress In Electromagnetics Research*, vol. 55, p. 307–333, 2005.

- [53] A. C. Ludwig, "The definition of cross polarization," *IEEE Trans. Antennas Propag.*, vol. 21, no. 1, p. 1973, 116–119.
- [54] W.-M. Boemer, W.-L. . Yan, A.-Q. Xi and Y. Yamaguchi, "Direct and Inverse Methods in Radar Polarimetry, Part I," in *Basic concepts of radar polarimetry*, Dordrecht, The Netherlands, Kluwer Academic, 1992, pp. 155-245.
- [55] J. P. Hamaker, J. D. Bregman and R. J. Sault, "Understanding radio polarimetry—Part I: Mathematical foundations," *Astron. Astrophys., Suppl. Ser.*, vol. 117, no. 1, p. 137–147, 1996.

1015

1016

1017

1018 **List of Tables**

1019

1020 **TABLE 1: CANOPY PARAMETERS FROM DESTRUCTIVE SAMPLING [48]**

1021

1022

TABLE 1: CANOPY PARAMETERS FROM DESTRUCTIVE SAMPLING [48]

Constituents		Average Parameters				
Types	Kinds	Length [cm]	Radius [cm]	Density [m ⁻³]	Dielectric Constant	Orientation Uniform
Trunks	T1	617.0	8.73	0.005	15.6+i3.8	Vertical
Primary Branches	B1	187.0	4.30	0.016	12.0+i2.9	20° - 50°
	B2	153.8	1.58	0.188	12.0+i2.9	10° - 60°
Secondary Branches	B3	63.6	0.98	0.734	12.0+i2.9	0° - 90°
	B4	48.1	0.45	1.933	12.0+i2.9	0° - 90°
Leaves	L1	Thickness 0.012	10.2	11.12	35.2+i5.3	0° - 90°

List of Figures:

Figure 1: Arbitrary Bistatic Antenna Configuration

Figure 2: Representation of a vegetated landscape.

Figure 3: Scattering from a single particle immersed in the slab of mean medium over a flat ground surface.

Figure 4: Scattering mechanisms and vector definitions for bistatic antenna configuration.

Figure 5: Unit scattering vector definitions.

Figure 6: Change of polarization basis (a) between transmitter and receiver. (b) between transmitter, ground, and receiver.

Figure 7: Antenna polarization definition: y-axis is always parallel to x-y ground plane. While the y-axis represents H-pol, the x-axis denotes V-pol and the z-axis represents boresight direction of the antenna.

Figure 8: Paulownia Stands [48]. Distributions of scatterers are illustrated on the right panel.

The scatterer kinds that are indicated by circles are primary branches or trunks that contribute the scattering while the others contribute the attenuation only.

Figure 9: Coherent and incoherent components of received power as a function of incidence angle and the receiver altitude.

Figure 10: Angular responses of NBRCS scattering mechanisms and specular reflectivity. The filled markers denote cross-polarization (RL) while the unfilled markers represent co-polarization (RR). The receiver altitude is 500 m and the first Fresnel response is considered.

Figure 11: (a) “Effective” NBRCS as a function of Fresnel zones at various heights for ideal (the nonfilled markers) and beam-limited (the filled markers) antennas. (b)-(d) are Fresnel zones and projected antenna footprint on the ground for receivers at various heights. The red ellipses (total of ten) are Fresnel zones while the black ellipse is antenna footprint.

Figure 12: The effect of diffuse contribution on the reflectivity of total reflected signal. While the arrow in the right panel indicates increasing altitude (20 m to 500 m) for the first Fresnel zone, the arrow in the left panel indicates increasing Fresnel zone indices (1 to 10) at a receiver height of 20 m.

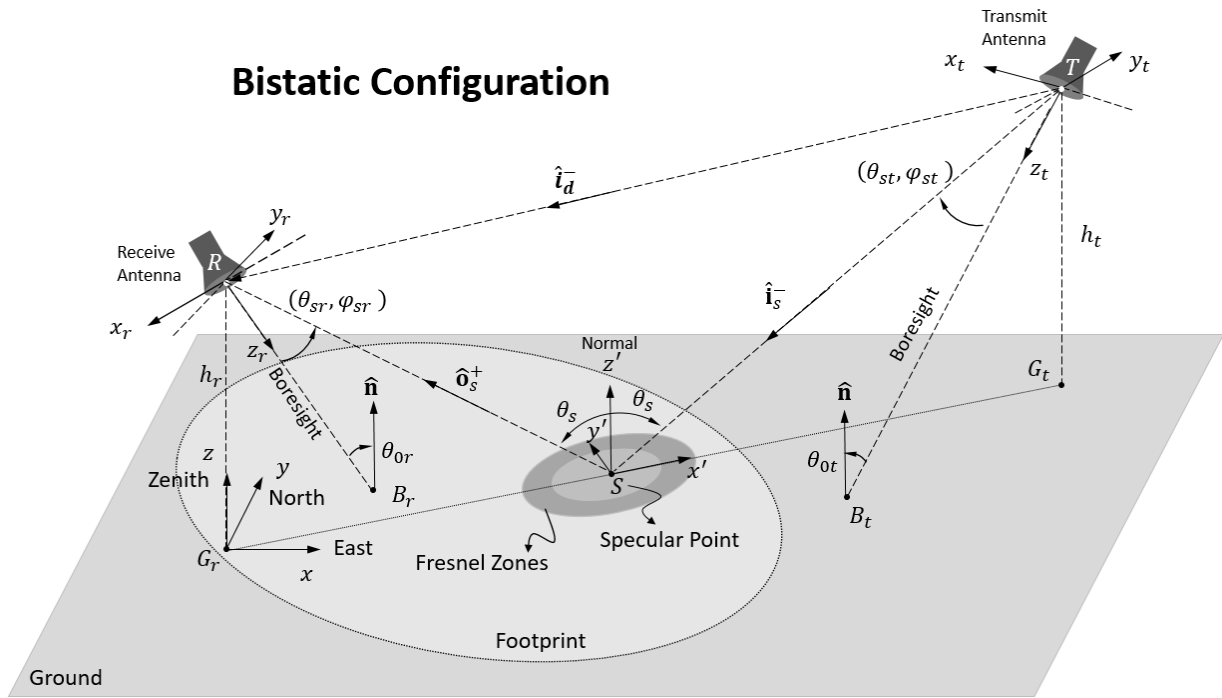


Figure 1: Arbitrary Bistatic Antenna Configuration

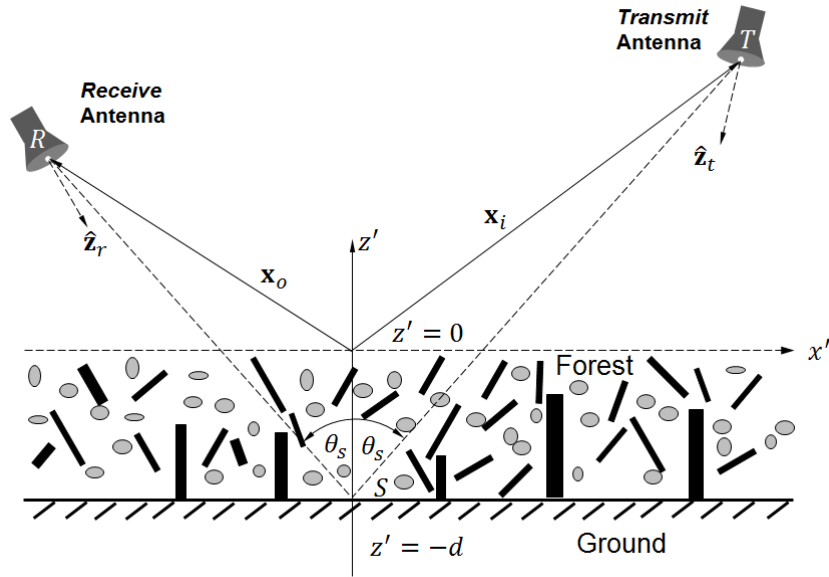


Figure 2: Representation of a vegetated landscape.

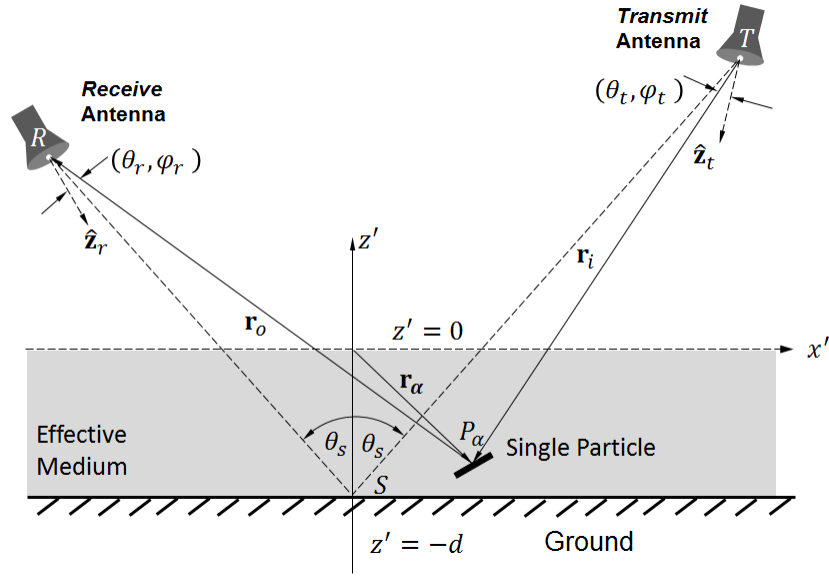


Figure 3: Scattering from a single particle immersed in the slab of mean medium over a flat ground surface.

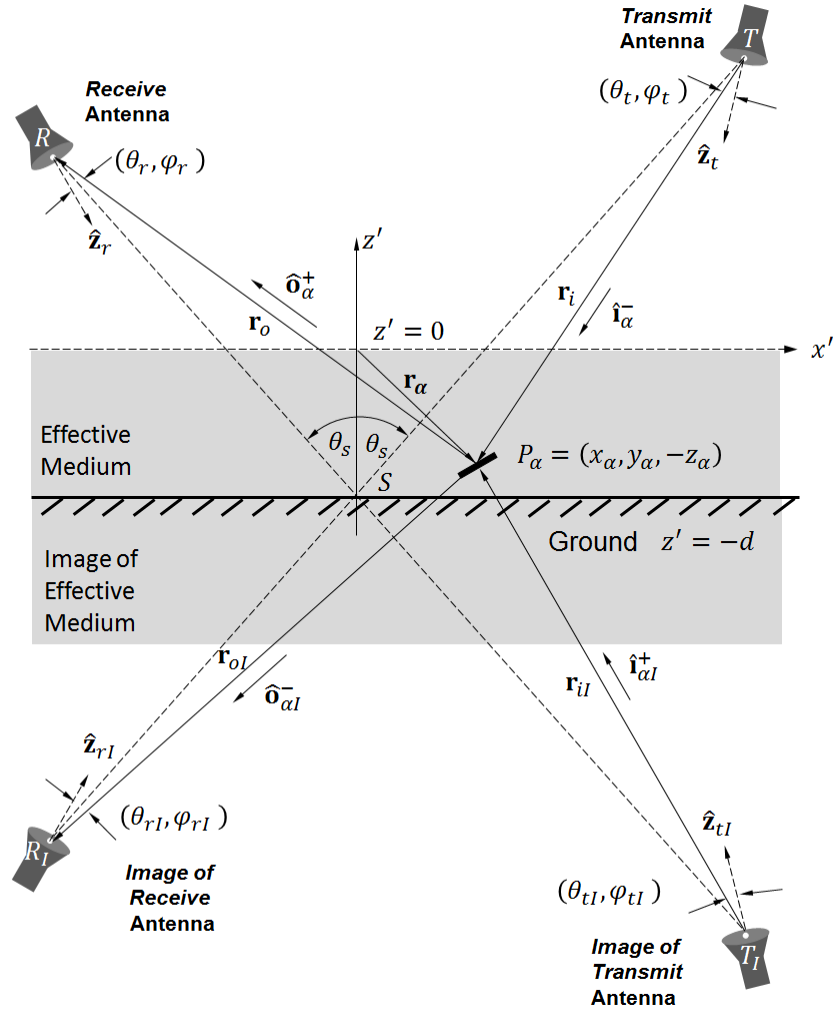


Figure 4: Scattering mechanisms and vector definitions for bistatic antenna configuration.

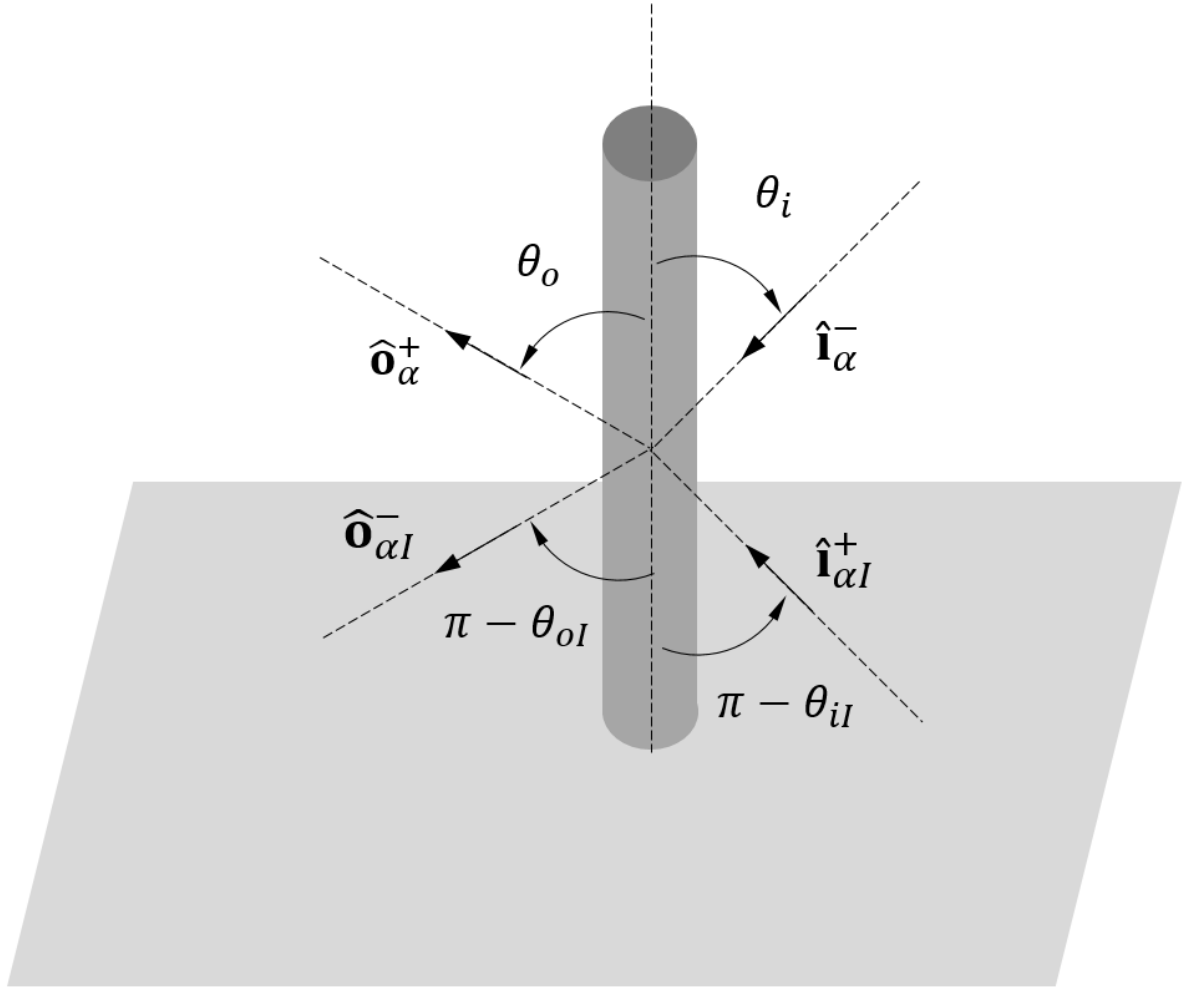
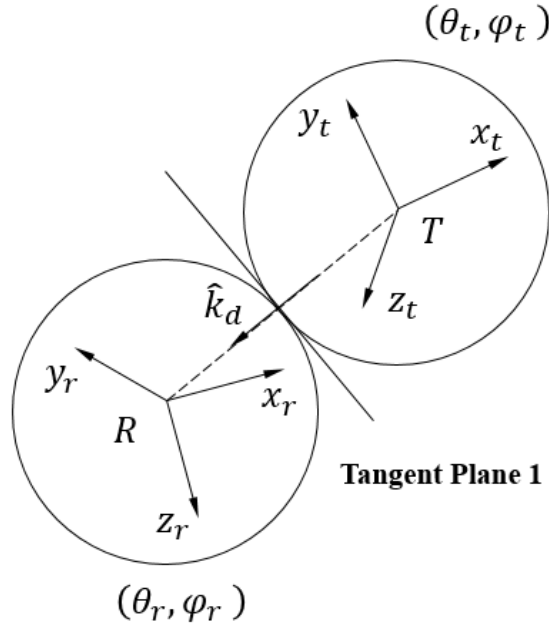
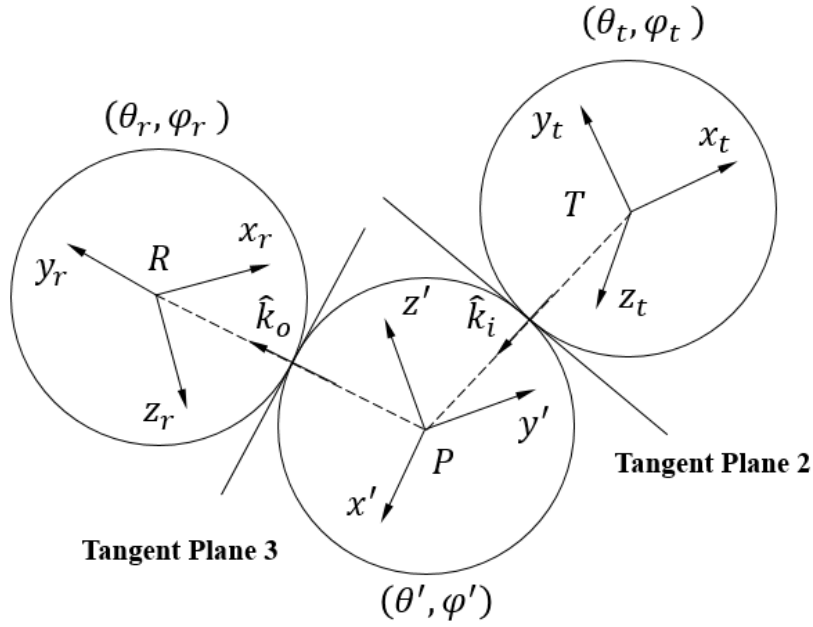


Figure 5: Unit scattering vector definitions.

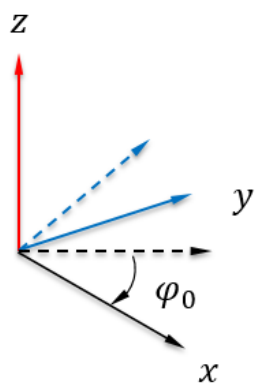
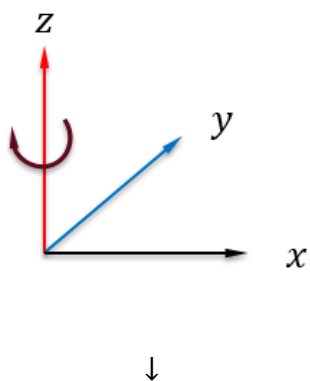


(a)

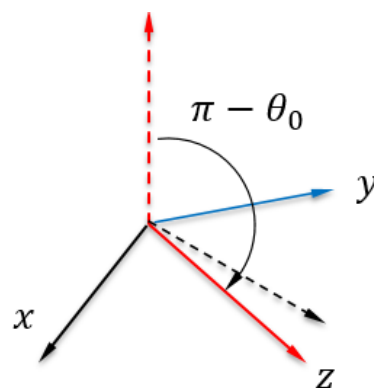
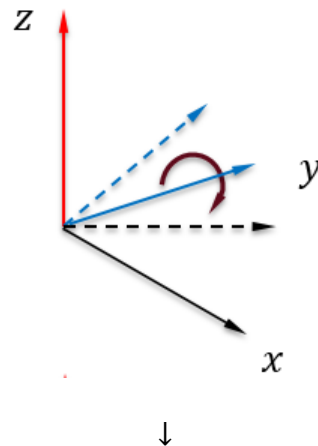


(b)

Figure 6: Change of polarization basis (a) between transmitter and receiver. (b) between transmitter, ground, and receiver.



(a) Antenna azimuth orientation:
Rotate about z-axis by φ_0



(b) Antenna incidence orientation: Rotate about
y-axis by $(\pi - \theta_0)$ in elevation

Figure 7: Antenna polarization definition: y-axis is always parallel to x-y ground plane. While y-axis represents H-pol, x-axis denotes V-pol and z-axis represents boresight direction of the antenna.

1094

1095

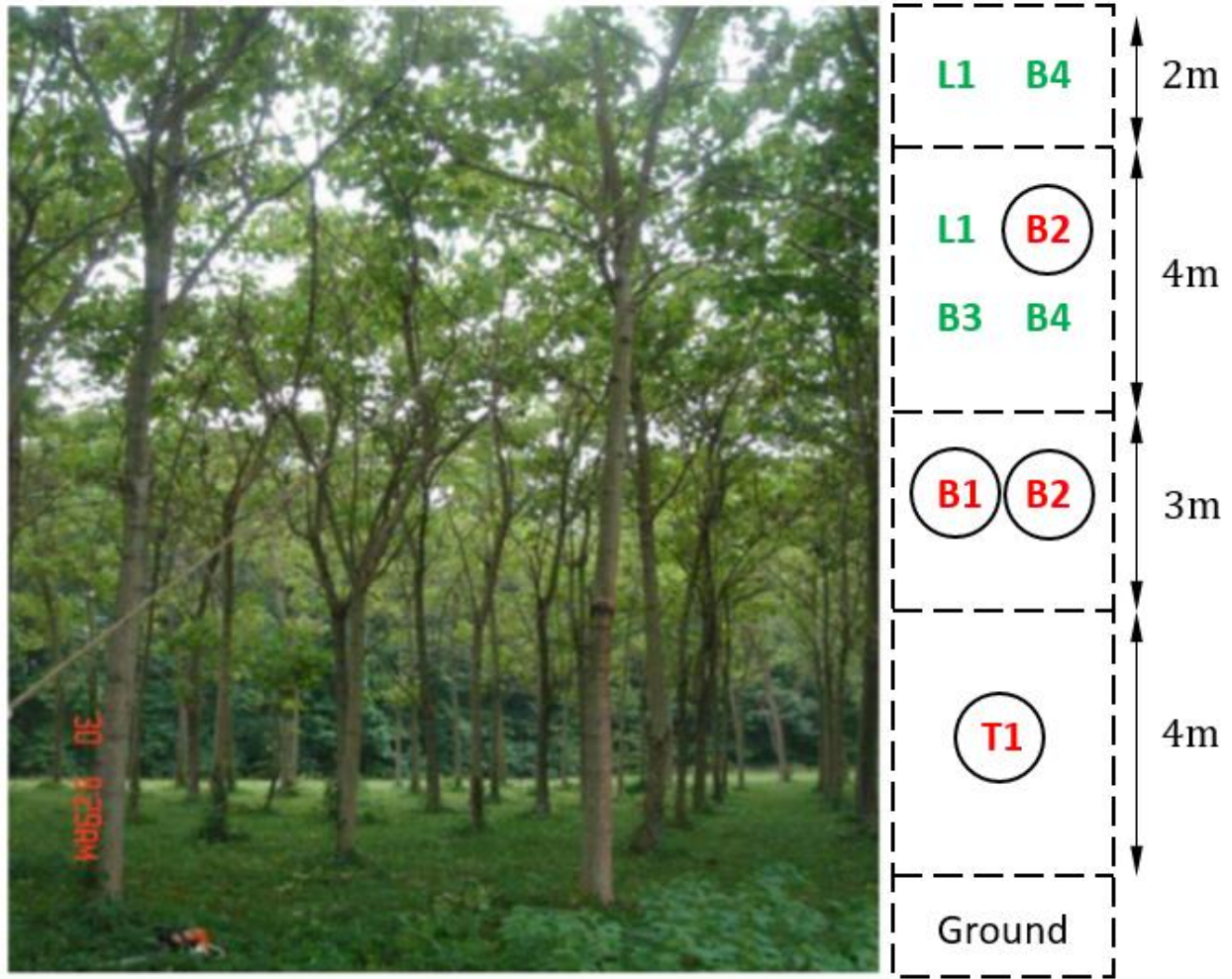


Figure 8: Paulownia Stands [48]. Distributions of scatterers are illustrated on the right panel. The scatterer kinds that are indicated by circles are primary branches or trunks that contribute the scattering while the others contribute the attenuation only.

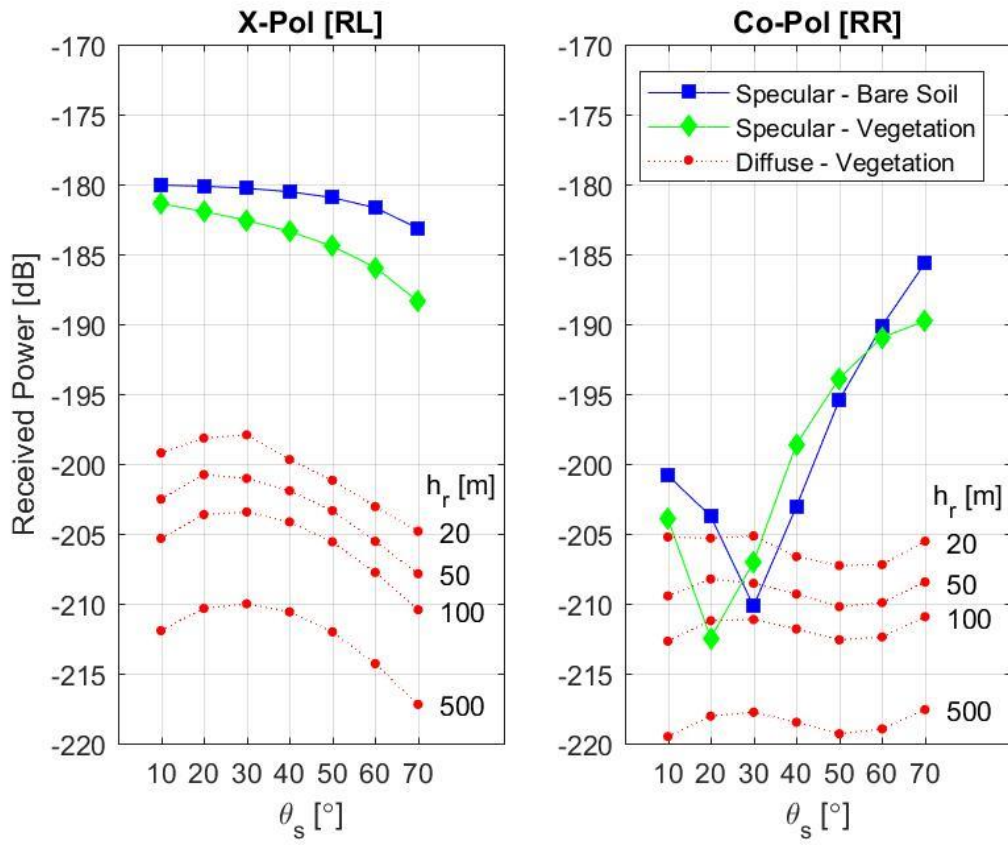


Figure 9: Coherent and incoherent components of received power as a function of incidence angle and the receiver altitude.

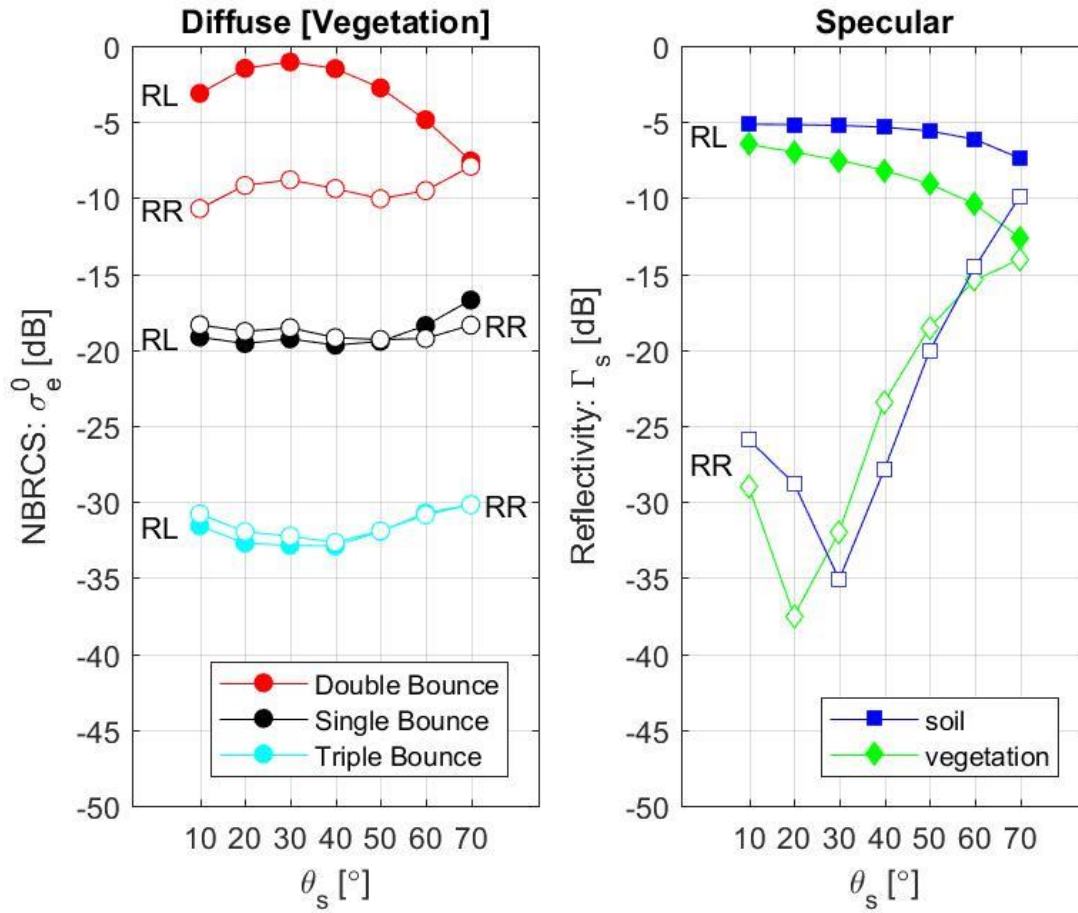
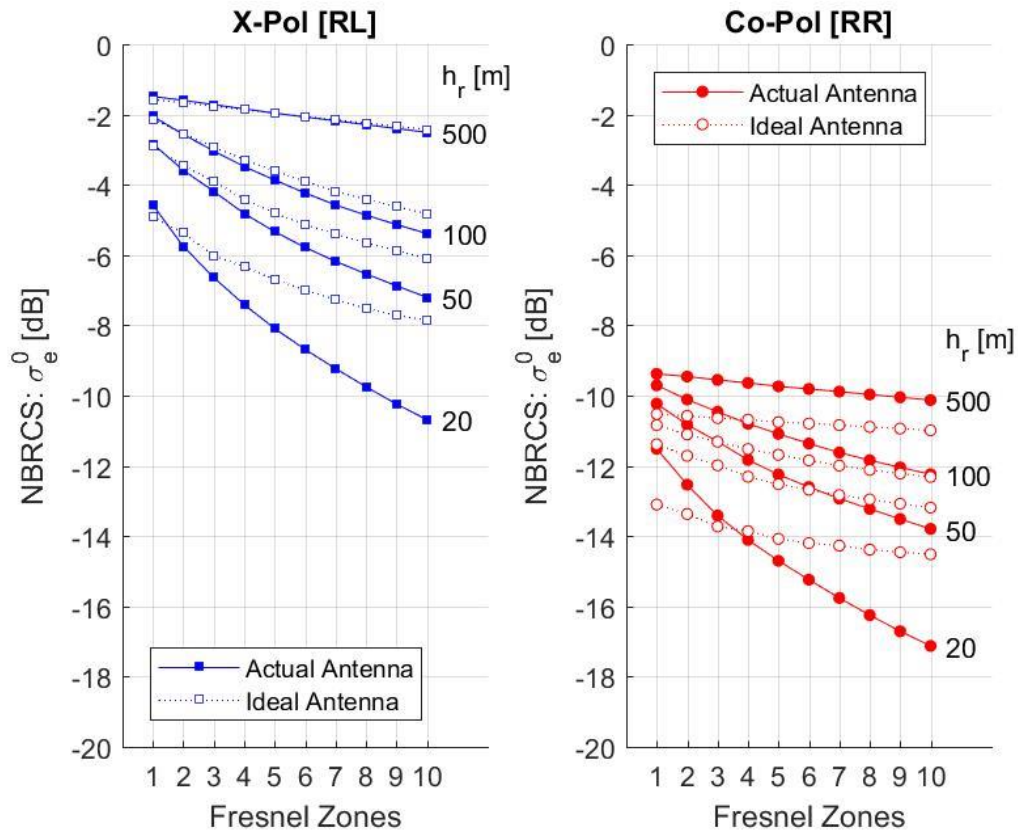
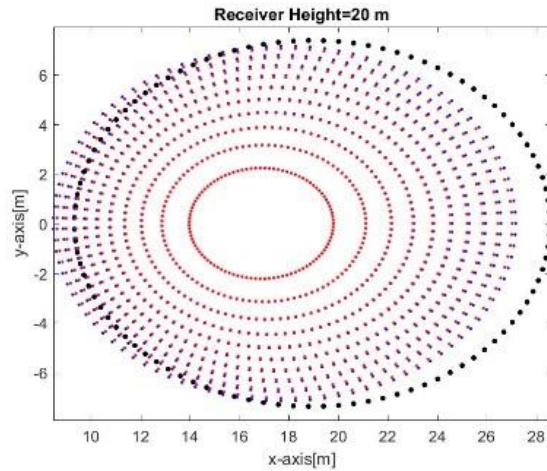


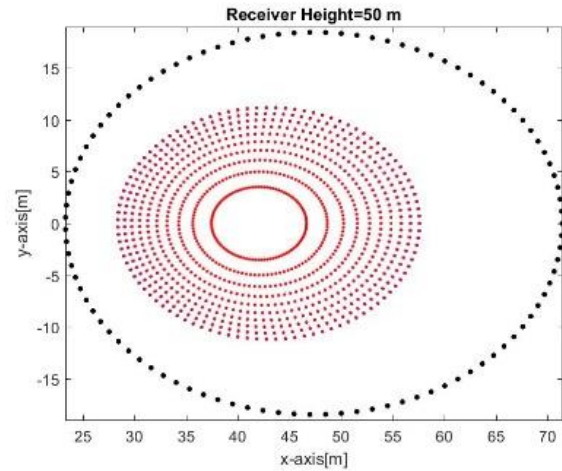
Figure 10: Angular responses of NBRCS scattering mechanisms and specular reflectivity. The filled markers denote cross-polarization (RL) while the unfilled markers represent co-polarization (RR). The receiver altitude is 500 m and the first Fresnel response is considered.



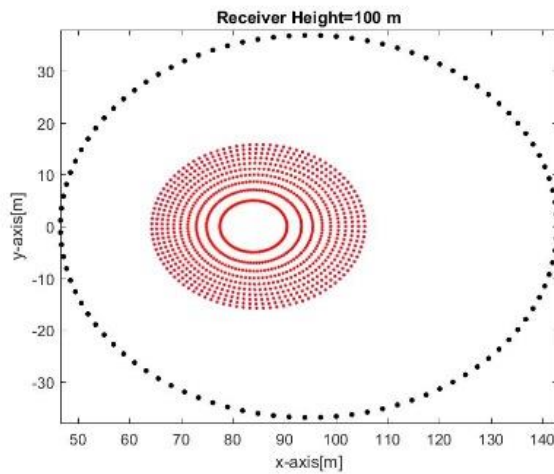
(a)



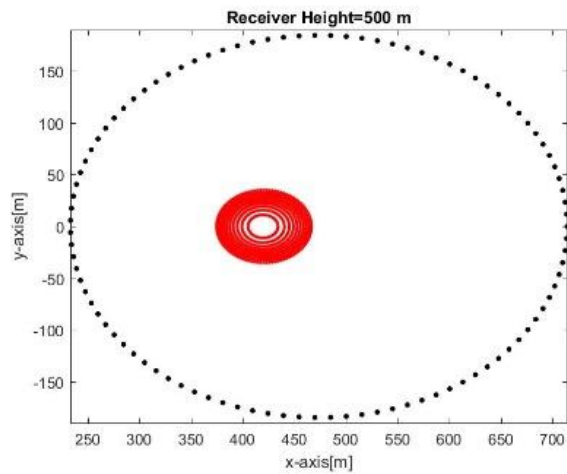
(b) 20 m



(c) 50 m



(c) 100 m



(d) 500 m

Figure 11: (a) “Effective” NBRCS as a function of Fresnel zones at various heights for ideal (the nonfilled markers) and beam-limited (the filled markers) antennas. (b)-(d) are Fresnel zones and projected antenna footprint on the ground for receivers at various heights. The red ellipses (total of ten) are Fresnel zones while the black ellipse is antenna footprint.

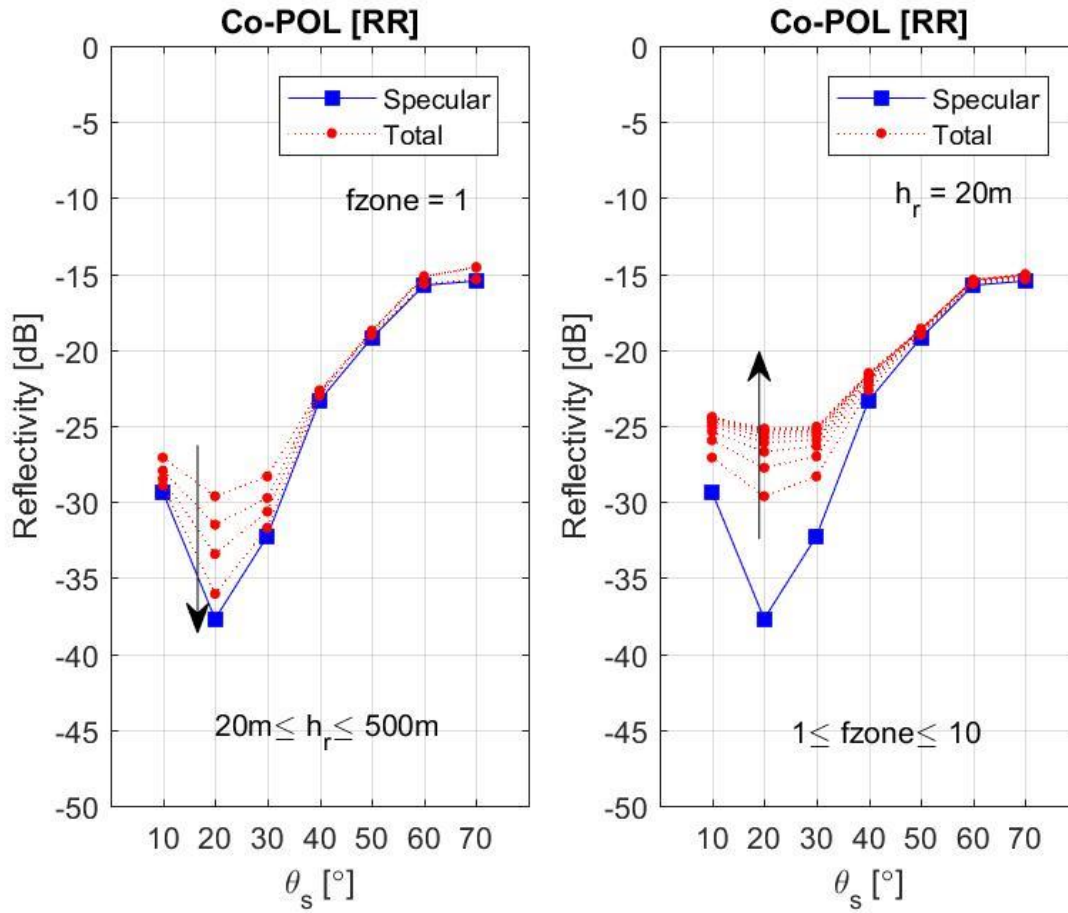


Figure 12: The effect of diffuse contribution on the reflectivity of total reflected signal. While the arrow in the right panel indicates increasing altitude (20 m to 500 m) for the first Fresnel zone, the arrow in the left panel indicates increasing Fresnel zone indices (1 to 10) at a receiver height of 20 m.